DEFECT EVOLUTION FROM LOW ENERGY GERMANIUM IMPLANTS IN SILICON

By

ANDRES FELIPE GUTIERREZ

A THESIS PRESENTED TO THE GRADUATE SCHOOL
OF THE UNIVERSITY OF FLORIDA IN PARTIAL FULFILLMENT
OF THE REQUIREMENTS FOR THE DEGREE OF
MASTER OF SCIENCE

UNIVERSITY OF FLORIDA

2001

To Dad, Mom, Guillermo, Javier

ACKNOWLEDGMENTS

The author would like to express his gratitude to his defense committee comprised of Dr. Kevin Jones, Dr. Mark Law and Dr. Robert DeHoff, for agreeing to guide him through this challenging yet rewarding learning experience. Specifically, the author thanks Dr. Jones, the chairman of the committee and research advisor, for his unwavering guidance, patience and enthusiasm as well as his thorough knowledge of the subject matter. Without these elements, this work would have been futile.

Furthermore, the author recognizes, and is grateful to, several people in the SWAMP group that contributed to the success of this work. Specifically, the author thanks Erik Kuryliw for the effective crash course in TEM analysis; Ibrahim Avci for assisting with UT-Marlowe simulations; Kevin Gable, Dena Wrigley and Jeannette Jacques for constant help in sample prep; Patrick Keys, Lance Robertson and Mark Clark for their expertise and very helpful and stimulating discussions. To these and the rest of the SWAMP group who provided an atmosphere of camaraderie and friendship, the author is very grateful.

The author further recognizes, admires and is ever grateful to his loving parents and brothers for their endless support and encouragement. From these special persons, the author has received the three priceless treasures of faith, hope and love. Finally, for this incredible opportunity, the author thanks God and His generous Providence.

TABLE OF CONTENTS

page

ACKNOWLEDGMENTS ... iii

ABSTRACT ... vi

CHAPTERS

1. INTRODUCTION ... 1

1.1 Background ... 1
1.2 Ion Implantation ... 2
1.2.1 The Need for Ultra Shallow Junctions ... 3
1.2.2 Implant Damage ... 4
1.3 High Energy Implants and Transient Enhanced Diffusion (TED) ... 5
1.3.1 Resulting Defects ... 6
1.3.2 Interstitial Evolution ... 6
1.3.3 Transient Enhanced Diffusion (TED) ... 10
1.4 The Case for Low Energy Implants ... 10
1.5 Preamorphization with Germanium ... 11
1.6 Objective and Approach of this Study ... 12

2. SAMPLE PREPARATION AND EXPERIMENTAL PROCEDURES ... 13

2.1 Overview and Sample Matrix ... 13
2.2 TEM Sample Preparation ... 15
2.3 Characterization and Analysis Techniques ... 16
2.3.1 TEM Analysis and Spectroscopic Ellipsometry ... 16
2.3.2 Image Analysis and Data Extraction ... 18
2.4 Experimental Procedure for the Energy Study ... 20
2.5 Experimental Procedure for the Dose Study ... 21

3. ENERGY AND DOSE DEPENDENCE ON DEFECT EVOLUTION ... 22

3.1 Results: 750 °C Experiment ... 22
3.2 Results: 825 °C Experiment ... 23
3.3 Results: Dose Experiment ... 25
3.4 Discussion ... 26

3.4.1 {311} Kinetics 27
3.4.2 Effect of Temperature and Energy 27
3.4.3 Effect of Dose at Low Energy 29
3.4.4 The Presence of Loops at Low Energy 30

4. CONCLUSIONS AND FUTURE WORK 52

4.1 Conclusions 52
4.2 Future Work 55

APPENDIX

PTEM IMAGES FOR THE ENERGY AND DOSE DEPENDENCE STUDIES 56

LIST OF REFERENCES 65

BIOGRAPHICAL SKETCH 68

Abstract of Thesis Presented to the Graduate School
of the University of Florida in Partial Fulfillment of the
Requirements for the Degree of Master of Science

DEFECT EVOLUTION FROM LOW ENERGY GERMANIUM IMPLANTS IN SILICON

By

Andres Felipe Gutierrez

May 2001

Chairman: Kevin S. Jones
Major Department: Materials Science and Engineering

The formation of highly doped, low resistivity ultra shallow junctions is a major challenge to the continued success of scaling trends of CMOS (complementary metal oxide semiconductor) devices. Advances in low energy ion implantation and thermal annealing techniques have helped prolong these trends, however a better understanding of the effects of the parameters involved with these processes is needed to attain the junctions required for next generation devices. This work will study the effect of implant energy and dose on the evolution of defects created via the annealing of the implant damage, thereby enhancing the understanding of interstitial evolution.

This experiment compares the defect evolution of 30, 10 and 5 keV, $1x10^{15}$ cm^{-2} amorphizing germanium implants in silicon upon annealing at 750°C using rapid thermal annealing (RTA) and conventional furnace for 10-120 seconds and 300-21600 seconds,

respectively. At the highest implant energy, dislocation loops and {311} type defects coexist at shorter anneal times, but eventually the {311}'s dissolve giving way to large stable dislocation loops. In sharp contrast, at the lowest energy level, only small unstable dislocation loops form but completely dissolve by 5400 seconds. This study was extended to a temperature of 825 °C, which yielded similar results. These observations indicate a new path of interstitial evolution, which would affect the physics of adverse dopant diffusion behaviors such as TED (transient enhanced diffusion).

Lastly, a dose study was carried out at the 5 keV implant energy to elucidate the effect of this parameter on defect evolution. Samples having a dose of $5x10^{14}$, $1x10^{15}$ and $3x10^{15}$ cm^{-2} were annealed at 750 °C and the time varied from 10 seconds to 21600 seconds. It was concluded that for this implant specie and conditions, dose does not have a significant effect on the damage produced from the implantation process and its evolution.

CHAPTER 1
INTRODUCTION

1.1 Background

The integrated circuit (IC) has ushered in an era of unforeseen technological advancements and fueled a thriving, worldwide industry. This industry has increasingly relied on the complementary metal oxide silicon (CMOS) structure to mass-produce IC's and this is now the dominant very large scale integration (VLSI) technology [1]. In the past two decades, the scaling of CMOS device dimensions has maintained the growth of the microelectronics and computer industry by increasing the transistor packing density and decreasing power consumption [2, 3]. It is crucial, if scaling is to continue, that certain challenges in the processing of sub –100 nm devices be overcome.

Several of these difficulties arise in the front end processes (FEP) of silicon wafers, including ultra shallow junction formation, leakage current with decreasing channel lengths, and the need for better inter-well isolation as packing density increases [2]. This introduction revolves around the issues of ultra shallow junction formation and the implantation/thermal budget regime it requires, with special emphasis on the implantation process itself, the subsequent formation of defects resulting from this process, and the evolution of these defects when subjected to specific annealing treatments.

1.2 Ion Implantation

Advances in ion implantation have made it the preferred method to introduce impurities into silicon to achieve reproducible concentration and depth profiles. The incident ions come to rest in the substrate material via electronic or nuclear stopping. In the former, energy loss occurs through the excitation and ionization of target electrons whereas the latter transfers kinetic energy to the target atoms oftentimes displacing them from their lattice positions and causing point defects such as Frenkel pair vacancies and interstitials. Figure 1.1 shows a schematic of these processes.

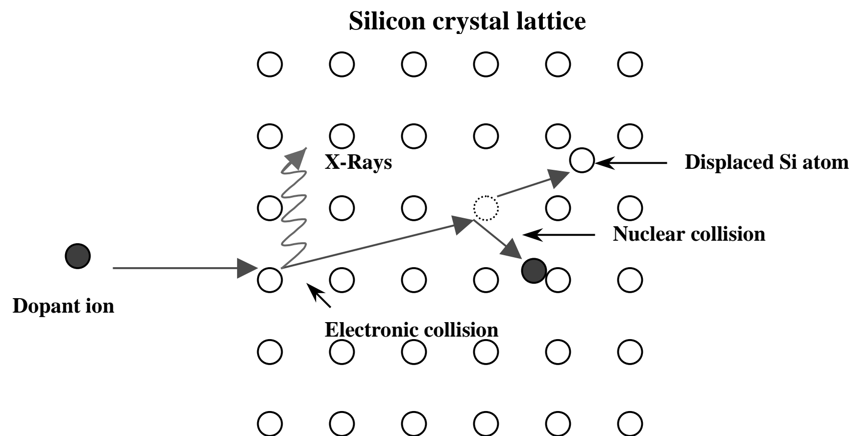

Figure 1.1 This figure shows a schematic of the displacement of a lattice atom by an incident dopant ion [4].

The resulting damage and channeling effects continue to hinder the doping and subsequent dopant activation requirements for next generation devices [4]. Further, upon annealing of this damage, interaction between the dopant ion and point defects created from the implantation process induce adverse diffusion and activation effects. Developments in low energy ion implantation and annealing techniques mitigate these

adverse effects but introduce complex thermal- and defect-induced reactions resulting from such shallow implants in silicon [5]. These include the backscattering of implanted ions and out-diffusion during implantation, and the limiting of dopant activation upon annealing. Finally, the near surface can affect formation, clustering, and annealing conditions of implantation damage [6].

These reactions raise new issues calling for more stringent specifications for ion implantation processes. Here, ion implantation is defined as the study of radiation damage effects, which depend on variables like substrate material, dose and energy, and annealing, or removal of this damage achieved through temperature uniformity and control across the wafer surface [5, 7].

1.2.1 The Need for Ultra Shallow Junctions

In order to continue device scaling, the formation of highly doped, ultra shallow, low-resistivity source/drain junctions is necessary. According to the SIA 1999 Roadmap these structures will need to achieve resistivities of 300 Ω/sq at <30 nm depths [2]. This will allow for longer effective channel lengths while minimizing high electric field short-channel effects.

Figure 1.2 illustrates the required junction depths, d_j, as a function of technology, characterized by its gate-length, L, and year of introduction in the lower and upper ordinate respectively. The squares, plotted on the right ordinate represent the energy of a Boron implant at a dose of $1x10^{15}$ cm^{-2}.

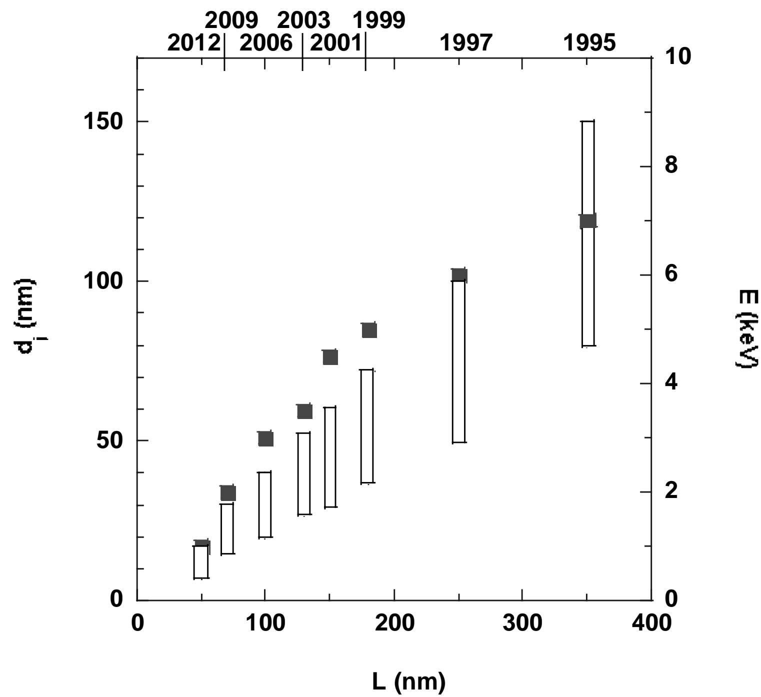

Figure 1.2 Required junction depth, d_j, (bars and left ordinate), at the channel as a function of technology, characterized by its gate-length, and year of introduction [8].

The drive to optimize ion implantation and subsequent annealing conditions to form these shallow junctions using established processes is evident due to the ease of integrating these steps in the process flow.

1.2.2 Implant Damage

The damage from the implantation process has been extensively studied [9-12], and a successful classification scheme of this damage has emerged [13]. The study of implant damage is necessary since it is closely related to the subsequent electrical properties of the implanted region [9]. Category I contains all the extended defects that form when the density of disorder from implantation is insufficient to produce an

amorphous layer. In contrast, Categories II, III, IV and V include defects that nucleate in the presence of an amorphous layer and its subsequent kinetics based on implant conditions and annealing treatments. In essence, the ability to predict whether an amorphous layer will be generated, and the depth of this layer form the basis for this scheme [13].

The scope of this study focuses on Category II defects in that the implant conditions of interest always produce an amorphous layer but inhibit the formation of Category III, IV and V damage. These extended range defects form beyond the amorphous/crystalline interface from the large concentration of interstitials present as a result of the implantation process. These defects can take the form of clusters, {311} defects, or dislocation loops. The morphology of each is now established [11, 12, 14], however the evolution behavior upon annealing is less well understood, especially at the technologically important low energies (i.e. less than 5 keV).

1.3 High Energy Implants and Transient Enhanced Diffusion (TED)

When injecting atoms into silicon at energies of ~100 keV, they generally come to rest in an interstitial space or get incorporated into interstitial complexes made up of the excess displaced silicon atoms. The nature of these is unknown, due to their small size and the inability to study them using conventional characterization techniques, although deep level transient spectroscopy (DLTS) has been used to identify electrically active clusters down to 50 Å in size [15]. In effect, these complexes render the dopant atoms electrically inactive. Hence, annealing treatments are necessary so that the interstitials

and/or interstitial complexes decrease in density, gradually increasing the number of implanted atoms occupying regular substitutional sites.

1.3.1 Resulting Defects

In general, secondary defects become large enough to observe via transmission electron microscopy (TEM) during post implantation annealing at temperatures exceeding 700 °C. Upon formation of an amorphous layer, these end-of-range (EOR) defects not only coarsen from the initially formed interstitial clusters but are also affected by the migration of the amorphous/crystalline interface as recrystallization occurs [12]. The kinetics of this interface have been studied by Drosd and Washburn [16] and Mader [11].

It should be noted that many EOR defect formation and evolution behavior trends have been linked to mutable experimental conditions, including implant species mass, dose, wafer temperature [17], dose rate [18], and implantation temperature [12, 19].

1.3.2 Interstitial Evolution

Figure 1.3 illustrates the generally accepted path of evolution for interstitials resulting from implantation of Si^+ and subsequent annealing. The implant can either be amorphizing or non-amorphizing; in this case the critical dose of amorphization is roughly $5x10^{14}$ cm^{-2} for Si^+ at low to medium energies (5-30 keV) [20]. It is evident that only two types of EOR defects are involved with this evolution – {311}'s and dislocation loops. The dissolution of these defects can lead to anomalous diffusion known as transient enhanced diffusion, or TED. This behavior will be detailed in Section 1.3.3.

Transmission electron microscope images of {311}'s and dislocation loops can be seen in Figure 1.4 a) and b), respectively.

This study will focus attention on dislocation loops and their behavior under a specific implantation/thermal budget regime. Therefore, a brief introduction of these defects will now be given.

Dislocation loop formation. For amorphizing implants, it was believed that dislocation loops nucleate, upon annealing, from primary defects residing in the crystalline silicon near the amorphous/crystalline interface [16]. However, this does not explain the large dose and mass dependence observed in the atoms bound by dislocation loops. This dependence is shown graphically in Figure 1.5 for Ge^+ and Si^+ implant species [13]. A more accurate explanation attributes loop formation to the release of silicon interstitials during {311} type defect dissolution resulting from specified post implantation annealing conditions [21, 22]. Consequently, the defect is extrinsic – it consists of Si-interstitial atoms stored in a metastable configuration [23]. For a thermodynamic explanation of dislocation nucleation, the reader is referred to the model proposed by Tan [14].

Dislocation loop stability. Loop stability very much depends on the conditions that resulted in their formation as well as subsequent annealing treatments. For example, a certain critical dose must be used in order to form stable loops [24]. Otherwise, it is argued, dislocations cannot exceed critical dimensions for stable growth due to lack of point defects from the implant. In this case, unstable loops nucleate but dissolve upon annealing.

Assuming an amorphizing implant and a high thermal budget, two types of dislocation loops are formed: perfect loops with a Burger's vector of a/2<110> and faulted loops with a Burger's vector of a/3<111>. These are viewed as 2-dimensional precipitates [23]. During annealing, a coarsening process known as Ostwald ripening takes place, resulting in the growth of large loops at the expense of smaller ones. Bonafos et al. give a thorough analysis of this process [25].

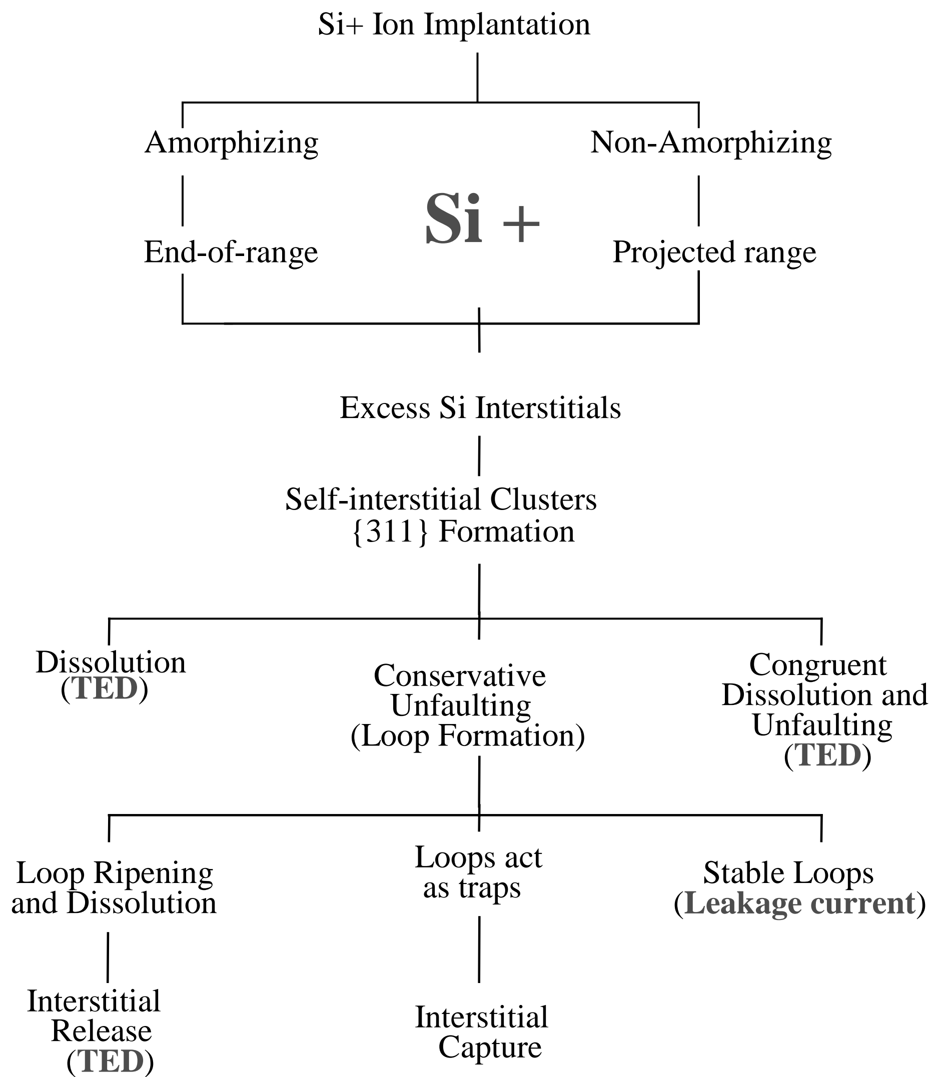

Figure 1.3 Illustration of interstitial evolution resulting from ion implantation into silicon and subsequent annealing.

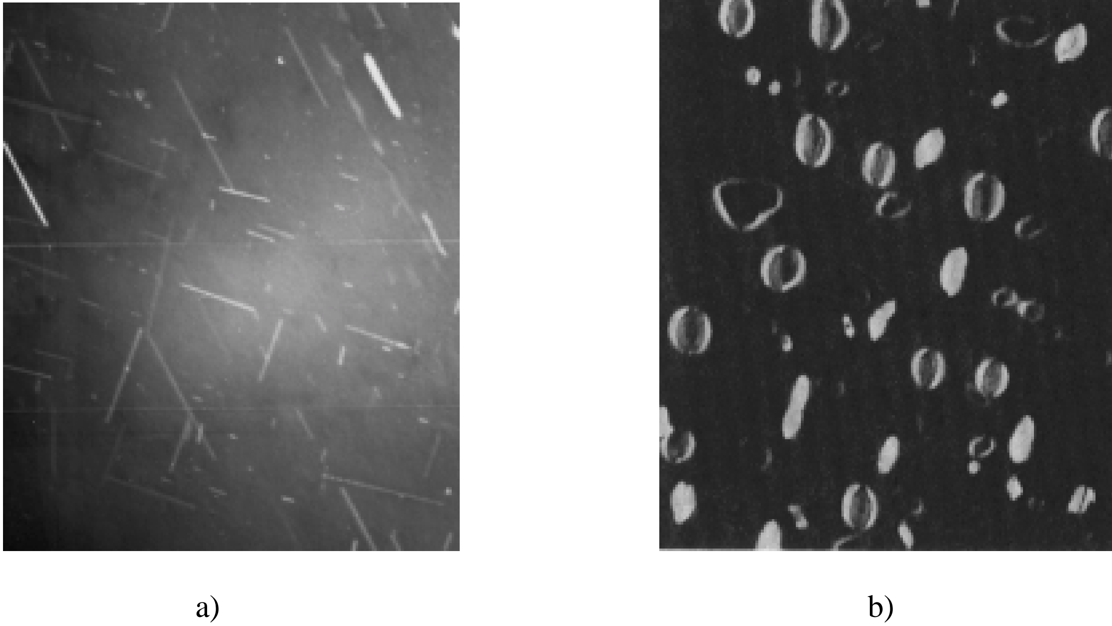

Figure 1.4 This figure shows the typical contrast of a) {311} type defects and b) dislocation loops for the weak beam dark field imaging condition.

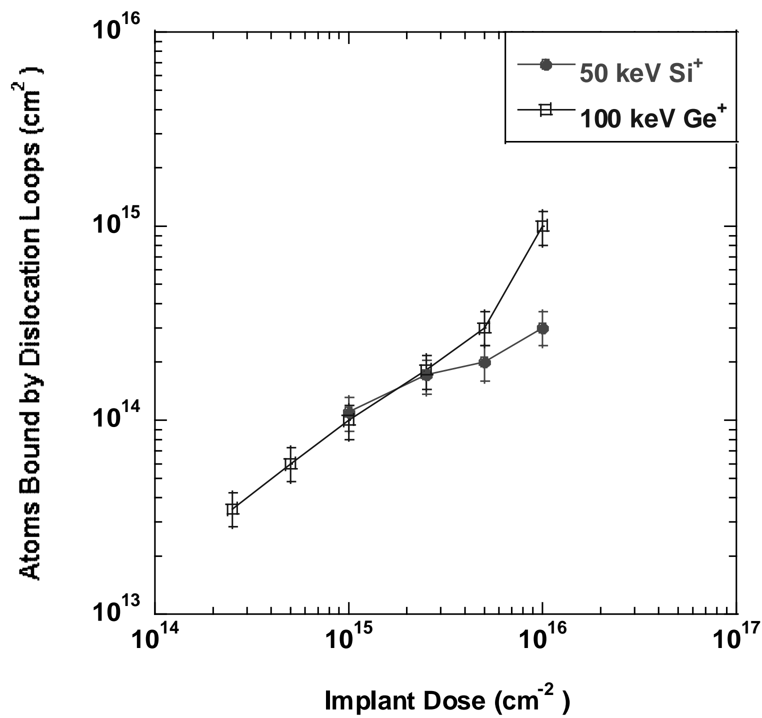

Figure 1.5 Graphical representation of the size dependence of dislocation loops with implant dose and mass [13].

1.3.3 Transient Enhanced Diffusion (TED)

TED and its reduction occupy a critical position in most technology roadmaps. This phenomenon, by which dopant atoms interact with the excess Si interstitials formed by ion implantation, greatly reduces dopant activation. These excess interstitials result from the dissolution of Category II EOR defects, as was reported by Eaglesham et al. [26], Jones et al. [27], and Cowern et al. [28]. Schematically, this was shown in Figure 1.3.

The enhanced diffusion of dopants such as Boron or Phosphorus can be as large as the implanted depth [29], which is many times higher than that predicted by process simulators, such as FLOOPS (Florida Object Oriented Process Simulator) [30], even in the low energy regime for certain conditions [31]. Other peculiar TED trends include a larger displacement at lower temperatures [32], and an increase in duration resulting from increased implant dose and energy [33]. Consequently, this poses a challenge to the formation of ultra shallow junction, and further studies are needed to elucidate optimum conditions for TED reduction.

1.4 The Case for Low Energy Implants

Recently, low energy implants have taken a central role in semiconductor processing. The low energy implant regime (single digit or sub-keV range) has experienced increased interest because of the expected ability to reduce the projected range of the implant and TED [20, 29, 34]. This will have the following consequences:

- The implanted layer is brought closer to the surface

- The ion straggling will be greatly reduced

The former will help bring about shallower junctions, while the latter increases the volume concentration of excess interstitials within the implanted layer [20]. However, the kinetics of extended range defects upon annealing change dramatically as a result of these effects.

1.5 Preamorphization with Germanium

Another technique that has gained much acceptance in the development of ultra shallow junctions is preamorphization of the silicon prior to dopant implantation [5, 35, 36]. By implanting Si^+ or Ge^+ (isoelectronic species with respect to the substrate) and amorphizing the surface prior to dopant implantation, several effects are attained:

- The elimination of channeling for implants at low energies
- The complete removal of residual damage upon annealing

The latter was achieved by Ajmera and Rozgonyi [37] and Ozturk et al. [36] by using germanium and adjusting the ion energy, dose and annealing temperature. Moreover, the appeal of a defect-free device lies in minimizing the junction leakage current that can occur as a result of Category II defects.

The use of germanium has other advantages over silicon as a preamorphizing agent. Since it is the heavier of the two species, marked differences in implantation kinetics result. For one, most of the energy loss occurs through nuclear collisions, inducing greater disorder in the silicon crystal, and a lower implant dose is required for amorphization.

Admittedly, low energy germanium preamorphization alone was not very effective in preventing the diffusion of excess Si interstitials under certain conditions [38], thereby inducing TED upon dopant activation. A greater knowledge of the defect kinetics from germanium implants is required for an understanding and prediction of the conditions for optimum TED reduction and ultra shallow junction formation.

1.6 Objective and Approach of this Study

This study will enhance the understanding of interstitial evolution at the technologically important low implant energy regime (< 5 keV) for a germanium preamorphizing implant. This is crucial for a comprehensive understanding of the kinetic behavior of EOR defects and the adverse processes they may induce upon annealing (i.e., TED). In turn, this understanding can be inputted into device process simulators for increased modeling accuracy.

The first experiment will compare the defect evolution, of germanium-implanted silicon at 5, 10 and 30 keV, upon annealing at 750°C using rapid thermal annealing (RTA) and conventional furnace. The results will be quantified from plan view transmission electron microscopy (PTEM) images, and relevant defect and interstitial behavior with respect to time will be extracted. The study will then be extended to 825 °C to elucidate the effect of temperature on defect evolution. Finally, the effect of dose variation will be reported for the lowest energy at 750 °C.

CHAPTER 2
SAMPLE PREPARATION AND EXPERIMENTAL PROCEDURES

2.1 Overview and Sample Matrix

In order to study the defect evolution from low energy germanium implants on silicon, it was necessary to discern appropriate experimental parameters, thereby leading to the most meaningful conclusions. These parameters include implant energy and dose, and temperature and time of anneals.

Czochralski-grown (001) Silicon wafers implanted with Ge^+ ions at room temperature were obtained from Varian Semiconductor Equipment, CA and SEMATECH International, TX. The implants were carried out at a 7° tilt to reduce channeling effects. Initially, Varian-implanted samples were used to obtain a “bird’s eye view” of defect behavior upon annealing at a variety of temperatures in a nitrogen atmosphere. This experimental setup, as well as the results from the plan view transmission electron microscopy (PTEM) images is shown in Table 2.1. On further analysis of these qualitative results, a new and more comprehensive sample matrix was developed. Table 2.2 outlines the experimental parameters of this sample matrix. The temperatures for this experiment were narrowed down to 750 and 825 °C, since it was evident that higher temperatures would yield defect-free structures for the lowest energy and dose, as seen in Table 2.1.

Table 2.1 Initial sample matrix to observe qualitative defect evolution behavior for 5 and 10 keV energies, and doses of $1x10^{15}$ cm^{-2} and $3x10^{15}$ cm^{-2}.

		5 keV $1x10^{15}$ cm^{-2}	5 keV $3x10^{15}$ cm^{-2}	10 keV $1x10^{15}$ cm^{-2}
750°C	60 min.	Very few defects	Very few defects	Few defects
	360 min.	No defects	No defects	Few defects
800°C	15 min.	Very few defects	No defects	Few defects
	180 min.	No defects	No defects	Few defects
850°C	5 min.	No defects	No defects	Very few defects
	60 min.	No defects	No defects	Few defects
900°C	5 min.	No defects	No defects	Very few defects
	60 min.	No defects	No defects	Few defects
950°C	5 min.	No defects	No defects	Few defects
	30 min.	No defects	No defects	N/A

Table 2.2 Experimental sample matrix in order to study defect evolution for 5, 10 and 30 keV germanium-implanted silicon.

750°C	5keV, $1x10^{15}$ cm^{-2}	10, 30, 60, 120 seconds in Rapid Thermal Anneal (RTA) furnace 5, 15, 30, 45, 60, 360 minutes in conventional furnace
	10keV, $1x10^{15}$ cm^{-2}	
	30keV, $1x10^{15}$ cm^{-2}	
825°C	5keV, $1x10^{15}$ cm^{-2}	5, 15, 30, 45, 60, 90, 360 minutes in conventional furnace
	10keV, $1x10^{15}$ cm^{-2}	
	30keV, $1x10^{15}$ cm^{-2}	

2.2 TEM Sample Preparation

Plan view transmission electron microscopy (PTEM) is appropriate to quantitatively study defect statistics [26], however cross section transmission electron microscopy (XTEM) was used to confirm the presence of an amorphous/crystalline interface and its depth for the as-implanted samples. It should be noted that in order to study defect evolution, PTEM was the primary method employed, hence the following description will detail PTEM sample preparation. For an in-depth review of XTEM sample preparation, the reader is referred to Camarce's Master Thesis [39].

Coring. A VCR Group Inc. coring drill, as well as a Gatan Inc. Ultrasonic drill, was used to cut 3 mm diameter discs from the sample 200 mm wafers. The lubricating medium was a 0.3 μm diamond-based slurry for the VRC drill, and a SiC-based cutting grit for the Ultrasonic drill.

Annealing. The next step involves the annealing of these discs. Specimens requiring 10-120 seconds were annealed in an AG Associates Heatpulse 410 rapid thermal annealing (RTA) system. For times above five minutes, a LINDBERG tube furnace was used. A 30 second push/pull procedure minimized thermal stresses. Lastly, an N_2 ambient was used in all annealed samples.

Chemical-Mechanical Planarization (CMP). After annealing, it was necessary to lap the samples down to an appropriate thickness (~100 μm) for TEM analysis. The cored sample was mounted, with crystal bond, to a South Bay Technology Model 150 lapping fixture, and thinned using a 0.15 μm Alumina powder-based polishing agent.

Chemical Etching. Subsequently, specimens needed to be punctured to enable the TEM beam to traverse the silicon and produce an image. Samples are mounted (shiny

side down) on a Teflon platform using wax (a small opening in the backside is left wax-free) and then a drip-etch of a 25% HF/ 75% HNO_3 solution is used to produce a small hole. Heptane is used to remove the wax from the sample.

2.3 Characterization and Analysis Techniques

The following sections describe the characterization and analysis techniques employed to quantify and tabulate the experimental results and stipulate corroboratory conclusions.

2.3.1 TEM Analysis and Spectroscopic Ellipsometry

A JEOL 200CX TEM was used to carry out all PTEM and XTEM analysis. In order to optimize defect imaging, a **g**220 weak beam dark field (WBDF) condition with **g**.3**g** diffraction was employed. As mentioned previously, PTEM was exclusively used to study defect evolution behavior for the given experimental parameters (i.e., implant energy, temperature, time and dose). These images can be seen in the appendix for the energy and dose experiments, respectively. XTEM was used to determine the amorphous/crystalline interface depth for the as-implanted 5, 10 and 30 keV implant energies at a dose of $1x10^{15}$ cm^{-2}.

The results were used to verify a series of measurements taken via ellipsometry using a J.A. Woollman multi-wavelength ellipsometer at a fixed angle of 75°. Three measurements were taken of each the 5, 10 and 30 keV, at $5x10^{14}$, $1x10^{15}$, $2x10^{15}$ and $3x10^{15}$ cm^{-2} doses, respectively. Figure 2.1 shows the XTEM results highlighting the depth of the amorphous/crystalline interface for the given implant energies. Figure 2.2 correlates these results with those obtained through ellipsometry.

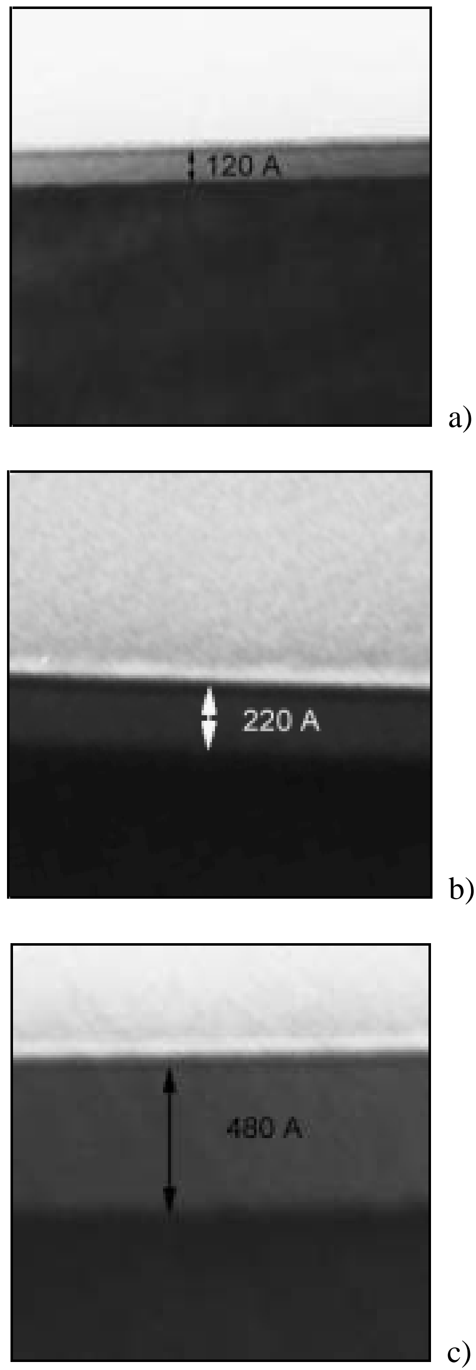

Figure 2.1 XTEM illustrating amorphous/crystalline layer thickness for the a) 5 keV, b) 10 keV and c) 30 keV implant energies at a dose of $1x10^{15}$ cm^{-2}.

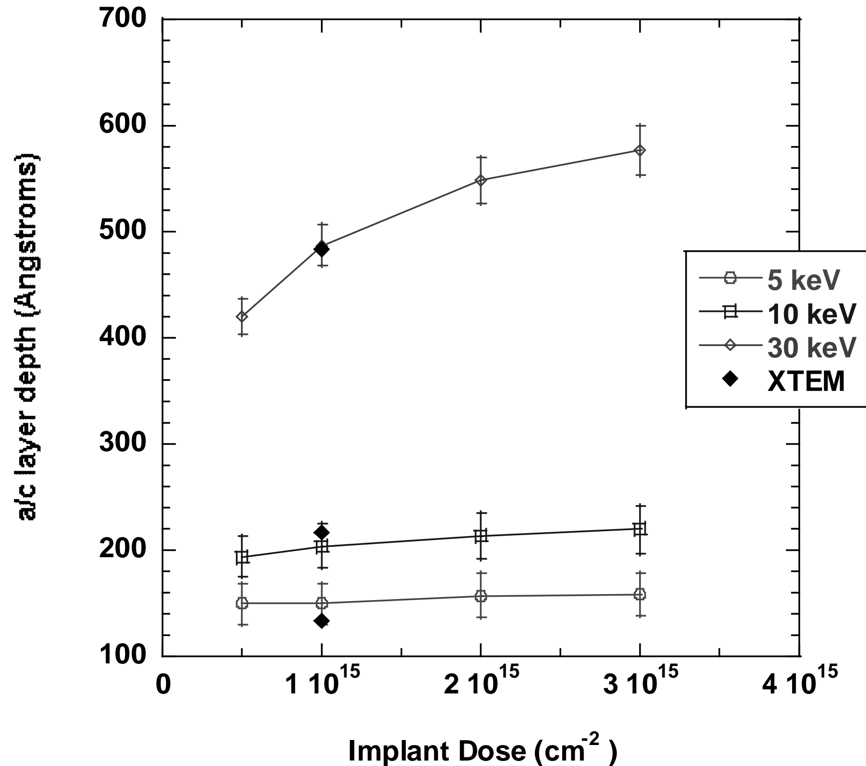

Figure 2.2 Correlation of the ellipsometry measurements for 5, 10 and 30 keV implant energies over a range of doses with XTEM results in order to verify a/c layer thickness. The error bars assume a 20 Å resolution error for the TEM.

2.3.2 Image Analysis and Data Extraction

Upon developing the PTEM images and enlarging to 150,000X, the prints were analyzed using appropriate counting methods to obtain meaningful statistics. The most commonly used methods are tracing without image processing and tracing with image processing. In general, tracing utilizes transparencies with defined areas to count defects from PTEM prints.

For the low energy (5 and 10 keV) time progressions at 750 and 825 °C, a tracing without image processing method was employed. By defining a square counting area (i.e., 2x2 cm^2, 3x3 cm^2 or 5x5 cm^2), the small defects at these energies were traced on a

transparency. Further, to increase the statistical significance of the counts, five randomly placed counts were used for each anneal time, and from the resulting average, a defect density was calculated. Subsequently, the trapped interstitials residing in the defects was calculated by multiplying the defect density times the number of interstitials per defect – a number obtained by multiplying the average area per defect by the packing density of the plane the defects inhabit (i.e., the {111} plane). This number is $1.6x10^{15}$ cm^{-2}. It should be noted that at these energies, the extended range defects observed were assumed to be dislocation loops. This assumption will be further addressed in Chapter 3.

Tracing without image processing was used to calculate defect density for the 30 keV time progressions, but tracing with image processing was used to calculate trapped interstitials since at this energy, *both* types of extended range defects, {311}s and dislocation loops, were present. This alternate procedure involved tracing the defects in 10x12 cm^2 rectangles on superimposed transparencies, for each type of defect respectively. The overlays were subsequently scanned into a computer and analyzed using the NIH v.1.61 image analysis software, yielding total area and total length, respectively for dislocation loops and {311} defects. To calculate the number of trapped interstitials in dislocation loops, the total area was converted into an area fraction by dividing by 120 cm^2 – the total area – and then multiplied by the packing density ($1.6x10^{15}$ cm^{-2}) of the plane in which these defects reside. To calculate the number of trapped interstitials in {311} type defects, the total length was adjusted by a factor of 1.56 (get source) to account for limitations in the counts available via PTEM. This adjusted length is then converted to the number of trapped interstitials in {311}s by multiplying it times the number of interstitials per unit length, assuming 26 interstitials per nm. These

results were plotted with respect to time and temperature to observe defect behavior trends and elucidate correlative conclusions.

Lastly, two software packages were employed to compare the experimental results. The first package is called **SRIM**2000 (the Stopping and Range of Ions in Matter), and calculates the net excess interstitial, or NEI, density for the given implant species and energies. **SRIM** is a group of programs, which calculate the stopping and range of ions (10 eV - 2 GeV /amu) into matter using a quantum mechanical treatment of ion-atom collisions. **UT-Marlowe** [40] was also used to calculate the NEI for the given implants. These results were compared to the experimentally calculated trapped interstitials. The results will be addressed in the discussion section of Chapter 3.

2.4 Experimental Procedure for the Energy Study

Following the matrix shown in Table 2.2, 5, 10 and 30 keV, $1x10^{15}$ cm^{-2} Ge^{+}-implanted samples were prepared for PTEM analysis. Annealing times were varied from 10 seconds to 360 minutes, and all anneals were carried out in a N_2 ambient. For the 10, 30, 60 and 120 seconds times, an RTA anneal was employed. For the 5, 15, 30, 45, 60, 180, and 360 minutes anneals, a conventional furnace was used.

The first set of results was gathered from the 750 °C isothermal anneals. Defect density and trapped interstitials evolution over time was monitored for the three energies. Subsequently, another isothermal progression was carried out at 825 °C for the three energies. Chapter 3 will relate and discuss these results.

2.5 Experimental Procedure for the Dose Study

In order to improve our understanding of EOR defect evolution upon annealing, it becomes necessary to study not only energy effects, but implant dose dependence. Accordingly, three doses were studied while keeping the implant energy constant at 5 keV. Samples of $5\text{x}10^{14}$, $1\text{x}10^{15}$ and $3\text{x}10^{15}$ cm^{-2} 5 keV Ge^{+}-implanted silicon were annealed for 10 seconds using an RTA furnace, while anneals for 5, 15, 30, 45, 60 and 360 minutes used a conventional furnace. All anneals were carried out in an N_2 ambient. The results of this study, including defect density and trapped interstitials over time, will be detailed and discussed at the end of Chapter 3.

CHAPTER 3
ENERGY AND DOSE DEPENDENCE ON DEFECT EVOLUTION

3.1 Results: 750 °C Experiment

PTEM micrographs illustrating the defect evolution behavior for the 5, 10 and 30 keV, $1x10^{15}$ cm^{-2} implant dose samples, annealed at 750 °C, are given in Appendix A, Figures A.1, A.2 and A.3, respectively for each energy. The results are quantified using the procedures outlined in Chapter 2 and plotted in Figures 3.1, 3.2 and 3.3, respectively for the 30, 10 and 5 keV implant energies. The graphs show defect density (in # of defects/cm^2) plotted with respect to time (in seconds) on a log-log scale.

Since at the highest energy, both {311} type defects and dislocation loops are present, separate defect evolution curves were used for each type of defect (Figure 3.1), as well as the overall defect evolution curve which includes both {311}'s and dislocation loops. Moreover, it was visually not possible to discern between defect types on anneals shorter than 900 seconds, hence these curves begin at this time. It is evident that with increasing anneal time, there is a sharp drop in the number of {311} defects until they 'disappear' or reach the TEM sensitivity limit of about $1x10^{7}$ cm^{-2} [41], whereas the loop population stabilizes and becomes the dominant defect type. This {311}-defect dissolution behavior is expected and well known, as was discussed in Chapter 1 and again will be addressed in this chapter's discussion.

Lowering the energy to 10 keV yields the graph in Figure 3.2. At this energy, only dislocation loop defects are observed, which at around 300 seconds begin to decrease in numbers with no apparent leveling off, even at 21600 seconds. Finally, at the lowest energy level, the defect evolution behavior (Figure 3.3) differs considerably in comparison to the higher energies, as shown in Figure 3.4. As in the 10 keV defect evolution, only dislocation loops are observed for the entire range of anneal times, but the unprecedented drop in defect density at a defined moment in time, specifically between 2700 and 3600 seconds, alludes to a sharp difference in the stability of these defects when compared to the higher energies. This is further illustrated in Figure 3.5, which depicts the trapped interstitials in the defects for the three energies. It should be noted that the reason data points are missing from the 30 keV curve in this graph is that, as mentioned earlier, it was visually not possible to differentiate between defect types for annealing times less than 900 seconds.

3.2 Results: 825 °C Experiment

PTEM micrographs illustrating the defect evolution behavior for the 5, 10 and 30 keV, $1x10^{15}$ cm^{-2} implant dose samples, annealed at 825 °C, are given in Appendix A, Figures A.4, A.5 and A.6, respectively for each energy. The results are quantified using the procedures outlined in Chapter 2 and plotted in Figures 3.6, 3.7 and 3.8, respectively for the 30, 10 and 5 keV implant energies. The graphs show defect density (in # of defects/cm^2) plotted with respect to time (in seconds) on a log-log scale.

As with the preceding temperature, the 30 keV Ge^+ implant annealed at 825 °C displayed both {311} type defects and dislocation loops, specifically at times longer than

300 seconds. Accordingly, individual curves for each defect type were included in Figure 3.6. The sharp decline of {311} defects at 900 seconds occurs sooner than for the 750 °C anneal. In contrast, the dislocation loops proportionally stabilize and become the dominant defect type in the structure.

As the implant energy is lowered to 10 keV, {311} defects are no longer observed, as in the case for the 750 °C, 10keV defect evolution. However, an interesting trend in the stability of the dislocation loops present is noticeable. Whereas at 750 °C for this energy (i.e., Figure 3.2), the defect evolution curve showed no sign of leveling off at high anneal times, at 825 °C the loops rapidly stabilize by 2200 seconds, acquiring a value of $6x10^8$ defects/cm^2, and remaining in the silicon indeterminately, as shown in Figure 3.7.

Finally, for the lowest implant energy of 5 keV, the defect evolution behavior is shown in Figure 3.8. It is similar to that of the 750 °C curve for this energy shown in Figure 3.3, but about two orders of magnitude lower. However, whereas the sharp drop in defect density occurred between 2700 and 3600 seconds for the 750 °C samples, it takes place between 900 and 2700 seconds for the 825 °C samples. This trend at the higher temperature is indicative of the increased instability of these defects.

For a better understanding of these trends at 825 °C, the defect densities and trapped interstitials for all three energies are given in Figures 3.9 and 3.10. Of particular interest, as illustrated in both graphs but especially in Figure 3.10, is the fact that there appears to be an implant energy threshold between 5 and 10 keV which defines and characterizes the stability of extended range defects, dislocation loops in this case, and the interstitials these defects contain. At an energy of 10 keV, dislocation loops coarsen

and grow to a certain size, at which time they neither seem to consume nor release interstitials. In contrast, at 5 keV, this stable configuration is never attained and the dislocation loops undergo complex, and as yet unknown, kinetic processes which lead to complete dissolution.

3.3 Results: Dose Experiment

PTEM micrographs illustrating the defect evolution behavior for the 5 keV, $5x10^{14}$, $1x10^{15}$ and $3x10^{15}$ cm^{-2} implant dose samples, annealed at 750 °C, are given in the Appendix, Figures A.7, A.1 and A.8, respectively for each dose. The results are quantified using the procedures outlined in Chapter 2 and plotted in Figures 3.11, 3.3 and 3.12, respectively for increasing implant dose. The graphs show defect density (in # of defects/cm^2) plotted with respect to time (in seconds) on a log-log scale.

It is evident from these graphs that the extended defects that form and evolve during annealing exhibit a degree of instability not seen at higher implant energies, regardless of the implant dose. This instability is characterized by the dissolution of the defects, small dislocation loops, beyond the TEM detection limit. Figure 3.13 further highlights the evolution of the interstitials trapped within these defects. At a defined point in time - apparently not dependent on implant dose - around 3600 seconds, the dislocation loops release the interstitials and dissolve. This is the first time such unusual behavior for dislocation has been reported. The following section will discuss, more in-depth, possible causes for these observations.

3.4 Discussion

Previous studies [22, 28] detail defect and interstitial evolution upon annealing for high energy, high dose implants. This is schematically shown in Figure 1.3 for a medium to high energy (i.e., 40-100 keV) Si^+ implant in silicon. With these conditions, interstitial evolution can generally be understood as a time dependent hierarchy of defects made up of interstitials. It begins with small precursor clusters, which nucleate into {311} type defects. At longer times these become a source of interstitials, which can drive either dislocation loop formation via unfaulting or enhanced dopant diffusion (i.e., transient enhanced diffusion) via dissolution. In turn, the dislocation loops undergo a coarsening process with time, becoming large and stable with high dissociation energies. It should be noted that the scope of this study excluded determining or characterizing the existence of precursor interstitial clusters.

In this study, this scheme was observed to be accurate for the highest energy germanium implants (i.e., 30 keV, $1x10^{15}$ cm^{-2}). From Figures A.3 and A.6 in appendix A, it is possible to qualitatively witness the specified evolution for the 750 and 825 °C anneals, respectively. Initially for very short anneal times, a high density of small defects is observed. The majority of these evolve into {311} type defects with time, but all the while coexist with a low density of dislocation loops. For longer times, the role of the {311}'s change from sink to source of interstitials, dissolving and consequently driving the growth of large, stable dislocation loops.

3.4.1 {311} Kinetics

The dissolution kinetics of these {311} defects has been plotted for both temperatures in Figure 3.14. Both curves exhibit a drop to the TEM detection limit of $6x10^{9}$ interstitials*cm^{-2}, which represents the complete dissolution of {311} defects. The problem that this number is arbitrary and ambiguous at best gives rise to a large error at these points, and this is graphically shown in the figure by adding a large error bar all the way up to $5x10^{11}$ interstitials*cm^{-2}. An equation describing the exponential decay of the trapped interstitials in the {311}'s is given in

$$Si_I(t)=Si_0*e^{-t/\tau} \qquad (1),$$

where Si_I is the number of interstitials present in {311} defects over time, Si_0 is the initial number of interstitials at time zero and τ is the time constant for the dissolution of {311} defects. From Figure 3.14, the parameter τ has been extracted for both temperatures yielding values of 6 and 40 minutes respectively for 825 and 750 °C using the TEM detection limit. Using the high value of the error bar in Figure 3.14, these time constants change to 16 and 86 minutes, respectively for 825 and 750 °C. The results from the first calculation closely agree with the values obtained by Camarce [39] when he studied 30 keV, $1x10^{14}$ cm^{-2} Si^{+} annealed at 800 and 750°C, which were 38.74 minutes and 5.79 minutes, respectively.

3.4.2 Effect of Temperature and Energy

To study the effect of temperature on defect behavior, interstitial density for 750 and 825 °C was plotted for the 30, 10 and 5 keV energy levels in Figures 3.15, 3.16 and

3.17, respectively. Qualitatively, it can be concluded that with increasing temperature, there is a decrease in the number of trapped interstitials. This can be explained by the faster diffusivity provided via the higher temperature.

Furthermore, the number of interstitials at time zero was extracted for each set of data by extrapolating to zero. Since the dissolution mechanisms for the dislocation loops present in the 10 and 5 keV implant energy levels is unknown, these values will only serve a qualitative purpose. The values extracted will be compared with the net excess interstitials (NEI) present, as computed by software simulation packages such as SRIM2000 and UT-Marlowe. It is assumed that the number of excess interstitials after an annealing time is approximately proportional to the initial number of interstitials created by the implantation process [42]. Hence, the purpose of this comparison (i.e., the experimentally obtained number of interstitials with the values calculated via simulation) is to test this proportionality.

Table 3.1 presents the number of interstitials at time zero calculated from experimental results and the NEI population simulated by TRIM and UT-Marlowe. These values are shown graphically in Figure 3.18. Large differences between the two simulations are attributed to two factors. First is the fact that these calculations are based on statistics and the subtraction of two very large numbers - the number of interstitials minus the number of vacancies produced by the implantation process. The other factor is the large error in these values due to the disproportionate influence that depth of the amorphous/crystalline interface has. By changing the depth 20 Å in either direction, the error associated with the XTEM measurements, the values changed by as much as 90 %. This influence can be seen in Figures 3.19 and 3.20, which show the profiles given by

TRIM for the 5, 10 and 30 keV implants magnified 20X, as concentrations given in units of atoms per ion-Å. The amorphous/crystalline layer depths used were 120, 220 and 480 Å, respectively for increasing energy, and are shown as dashed lines in Figure 3.19 and as the vertical ordinate itself in Figure 3.20. Integrating the area under each curve from the amorphous/crystalline depth and multiplying by the dose yields the NEI population. It becomes apparent that moving this line will drastically change the area under the curves bounded by this parameter, especially in the case of the lowest energy.

Table 3.1 Interstitials at time zero (in units of $\#/cm^2$) calculated from experiments and simulations for the 5, 10 and 30 keV Ge^+ implants.

		5 keV	**10 keV**	**30 keV**
Experimental	750°C	$3.7x10^{13}$	$9x10^{13}$	$7.5x10^{13}$
	825°C	$1.17x10^{12}$	$1.2x10^{13}$	$2.0x10^{13}$
TRIM		$1.3x10^{15}$	$1.0x10^{15}$	$1.5x10^{15}$
UT-Marlowe		$2.6x10^{14}$	$1.7x10^{14}$	$2.8x10^{14}$

3.4.3 Effect of Dose at Low Energy

Previous studies [20] report a dose dependence on the formation and evolution of interstitials upon annealing of low energy implanted silicon. This is summarized in Figure 3.21, which illustrates interstitial behavior as a function of time of 5 keV, $1x10^{14}$ and $3x10^{14}$ cm^{-2} Si^+ implants annealed at 750 °C. These results disagree with those obtained in this study, where, according to Figure 3.13, no significant difference in interstitial evolution occurs by varying the dose of low energy implants. Several things

to note concerning this discrepancy include, first of all, the difference in implant specie, from Si^+ to Ge^+. Furthermore, the doses used are roughly an order of magnitude less than those used for this study, save the $5x10^{14}$ cm^{-2}. In fact, the $1x10^{14}$ cm^{-2} was not amorphizing and the $3x10^{14}$ cm^{-2} slightly exceeded the amorphization threshold. Lastly, the study reported that all the interstitials counted came from {311} type defects, whereas in this work, only dislocation loops were present at the lowest energy level.

3.4.4 The Presence of Loops at Low Energy

The last point mentioned above merits further discussion. A similar study by the same authors [29] likewise reported that for the given implant conditions (i.e., 5 keV, $3x10^{14}$ cm^{-2} Si^+ implant), only {311} defects were observed with a negligible density of dislocations loops, despite the expectation that these would dominate the damage landscape. They conclude that the dissolution kinetics of the {311}'s, which result in the release of interstitials, continues to drive enhanced diffusion phenomenon.

In contrast, this work has consistently shown that the only observable defects at the lowest energy studied (5 keV) were small, unstable dislocation loops, which dissolved within a narrow time window, regardless of dose or temperature. These loops did not nucleate from the dissolution of {311} type defects. It is therefore possible that the interstitials resulting from the given experimental conditions could have an alternate path of evolution than the one generally accepted for higher energy implants, as mentioned at the beginning of this discussion.

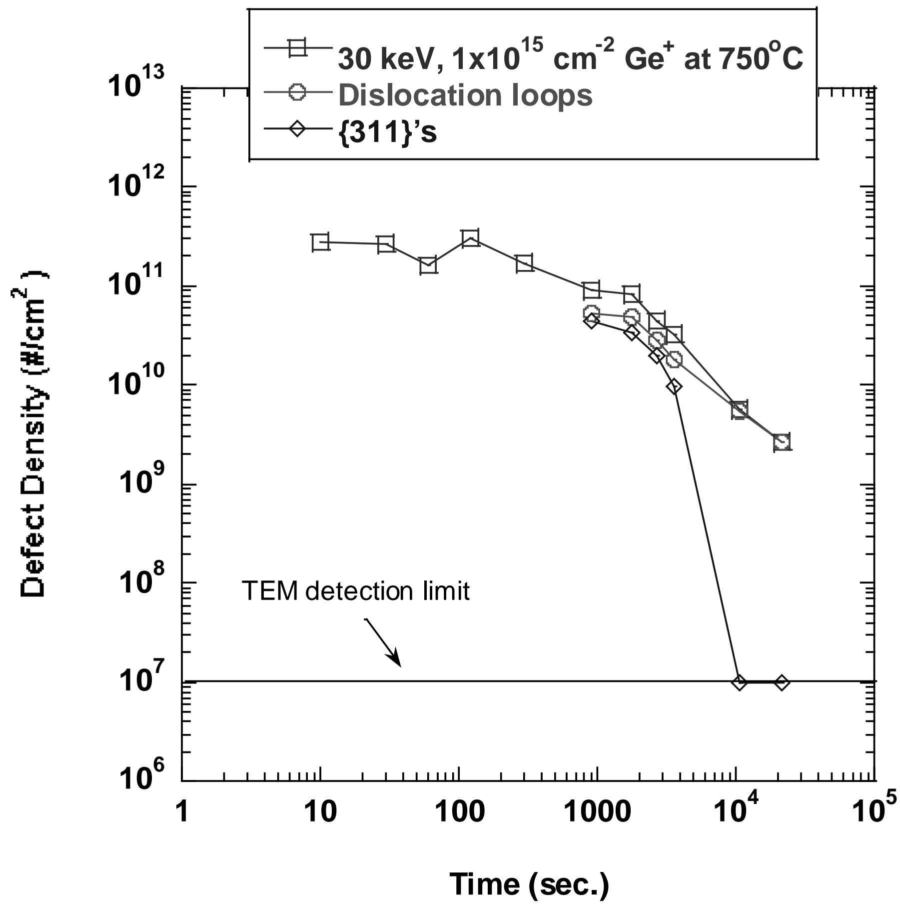

Figure 3.1 Defect evolution from a 30 keV, $1x10^{15}$ cm^{-2} Ge^{+} implant on silicon. For longer times, the defects were identifiable and counted separately in blue and red for {311} defects and dislocation loops respectively.

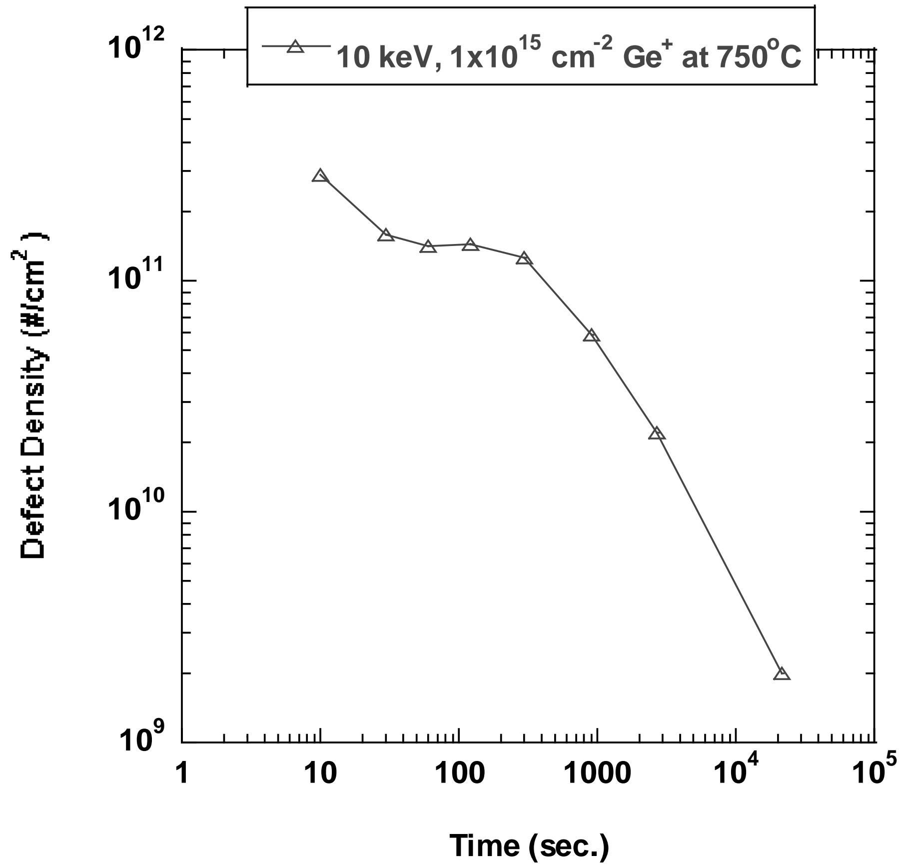

Figure 3.2 Defect evolution from a 10 keV, $1x10^{15}$ cm^{-2} Ge^{+} implant on silicon.

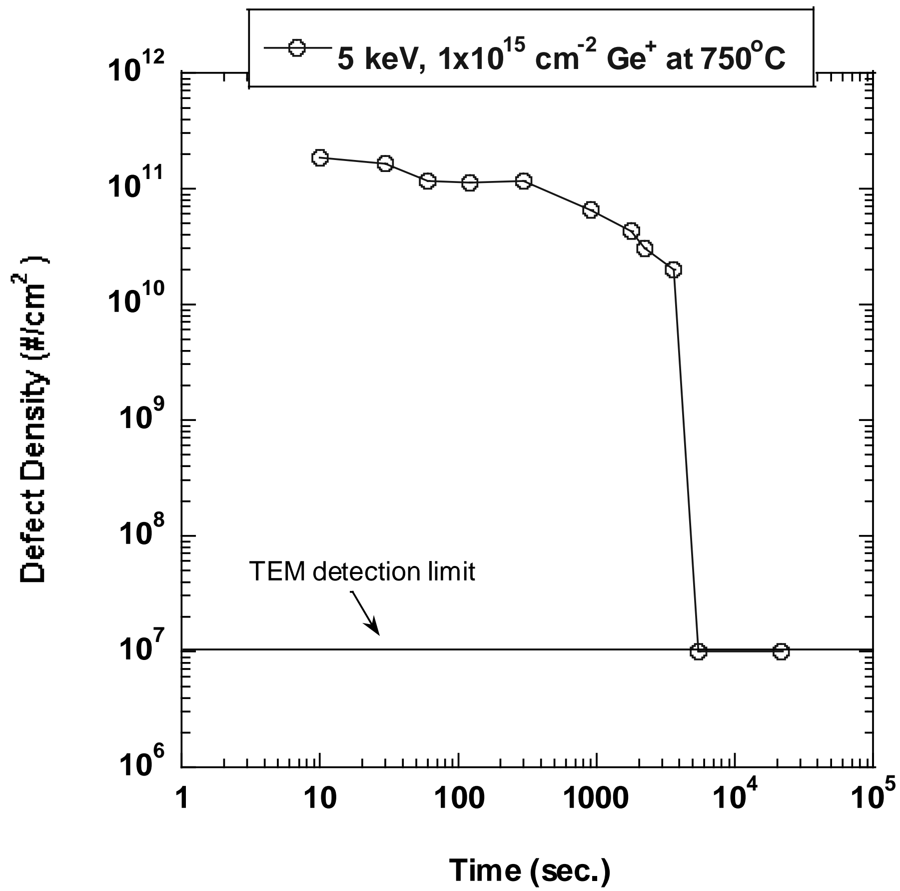

Figure 3.3 Defect evolution from a 5 keV, $1x10^{15}$ cm^{-2} Ge^{+} implant on silicon.

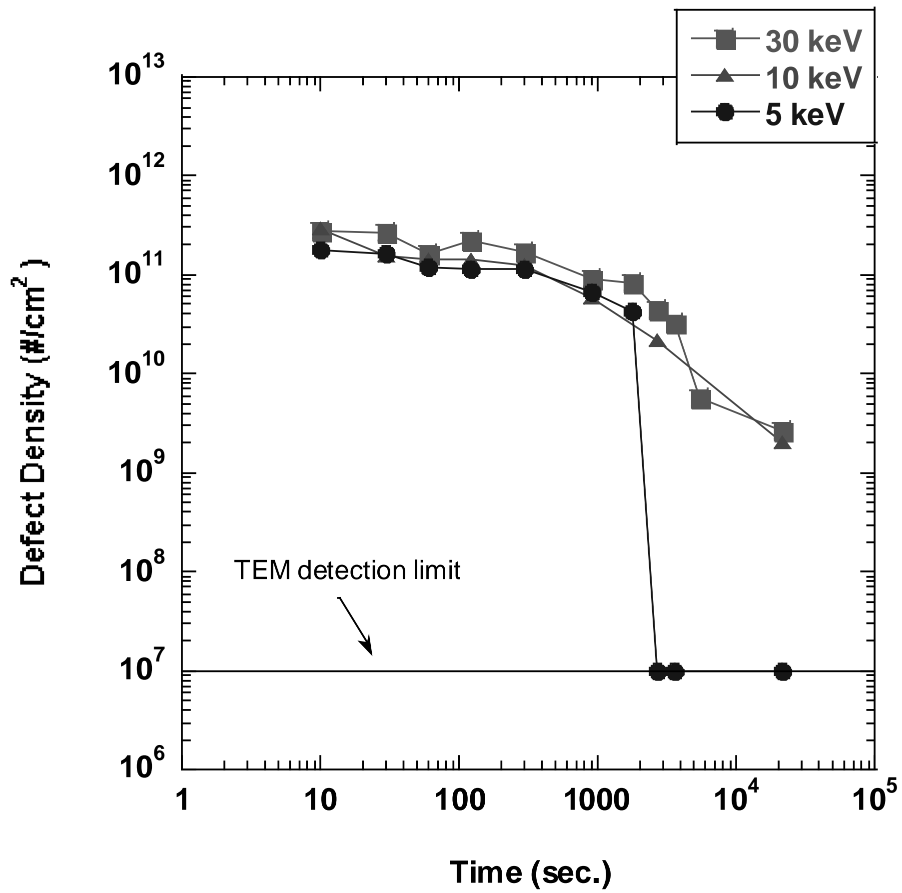

Figure 3.4 Combined defect density evolution for the 5, 10 and 30 keV $1x10^{15}$ cm^{-2} Ge^{+} samples annealed at 750 °C.

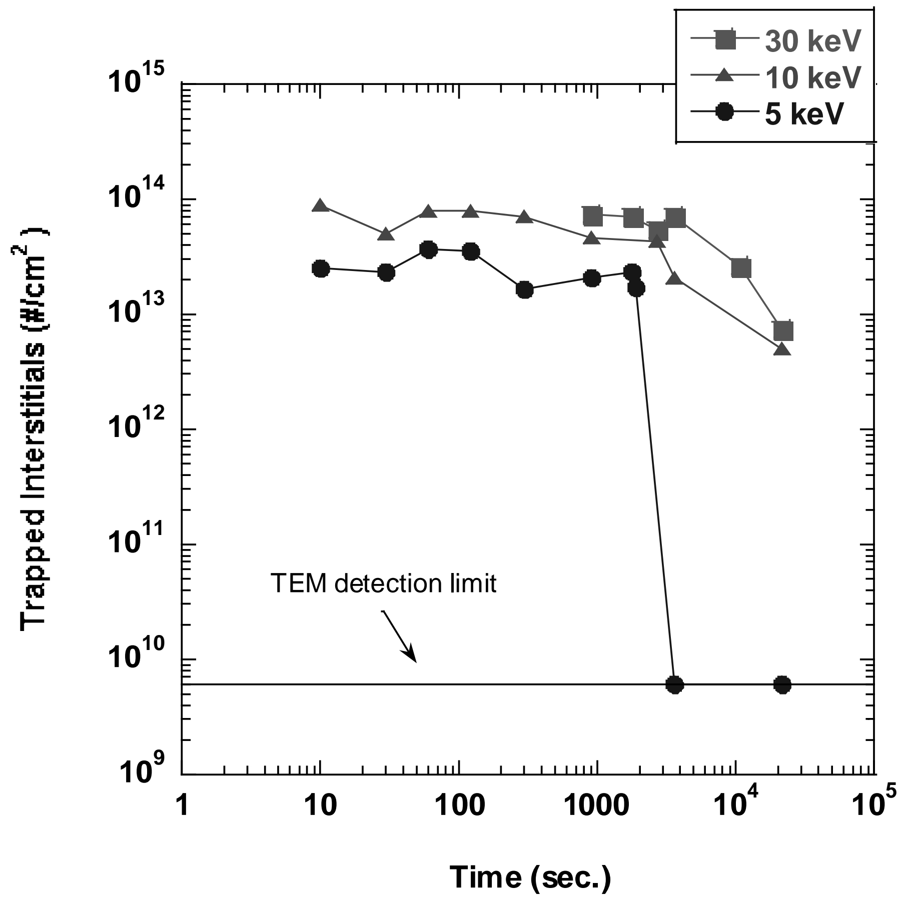

Figure 3.5 Trapped interstitials for defects from 5, 10 and 30 keV $1x10^{15}$ cm^{-2} Ge^{+} implants annealed at 750 °C.

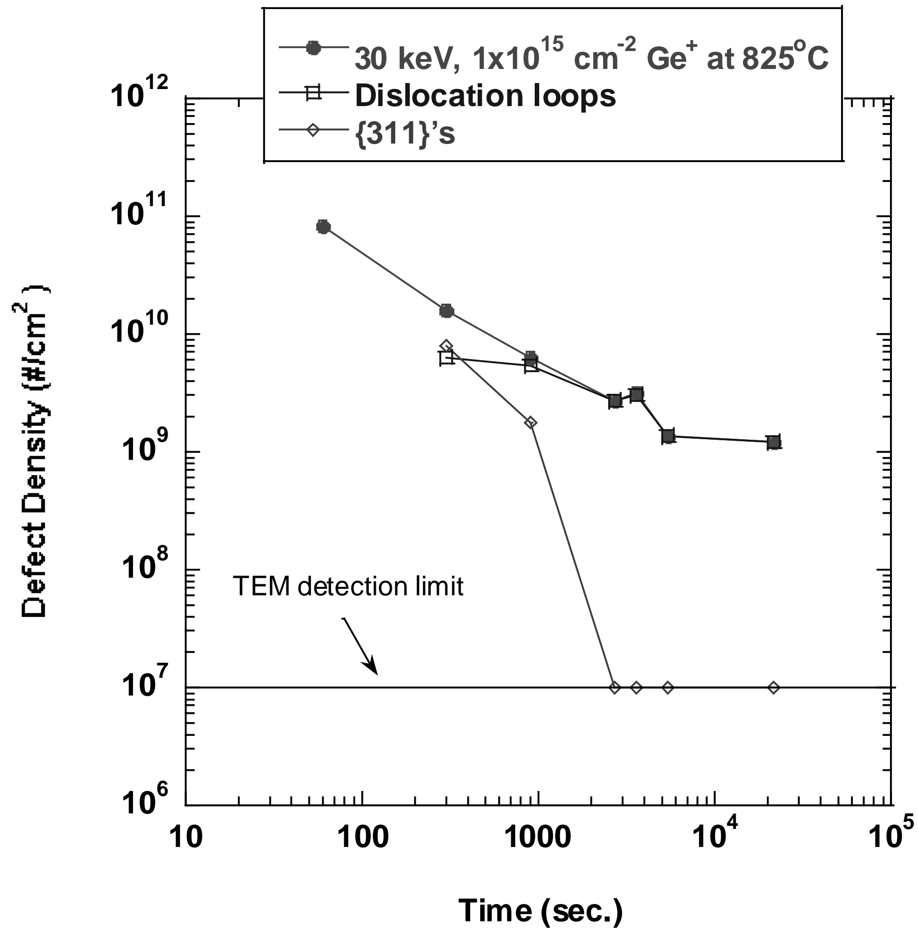

Figure 3.6 Defect evolution from 30 keV, 1×10^{15} cm^{-2} Ge^{+} implant at 825 °C. For longer times, the defects were identifiable and counted separately in blue and red for {311} defects and dislocation loops respectively.

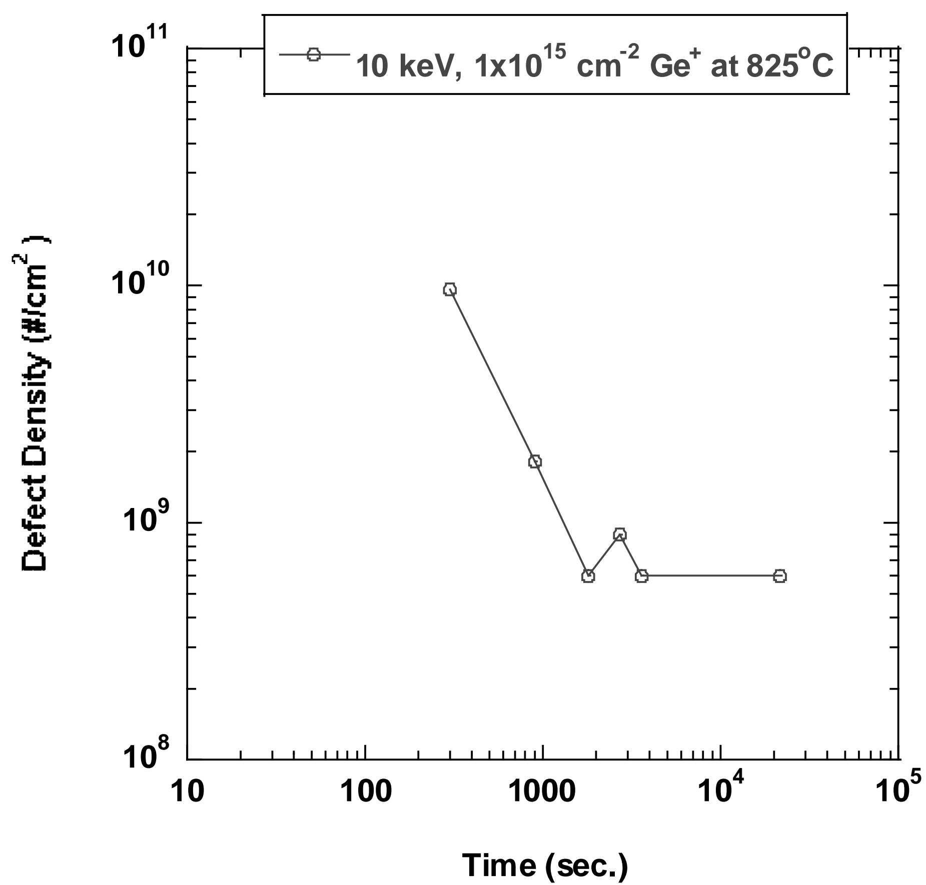

Figure 3.7 Defect evolution from 10 keV, $1x10^{15}$ cm^{-2} Ge^{+} implant at 825 °C.

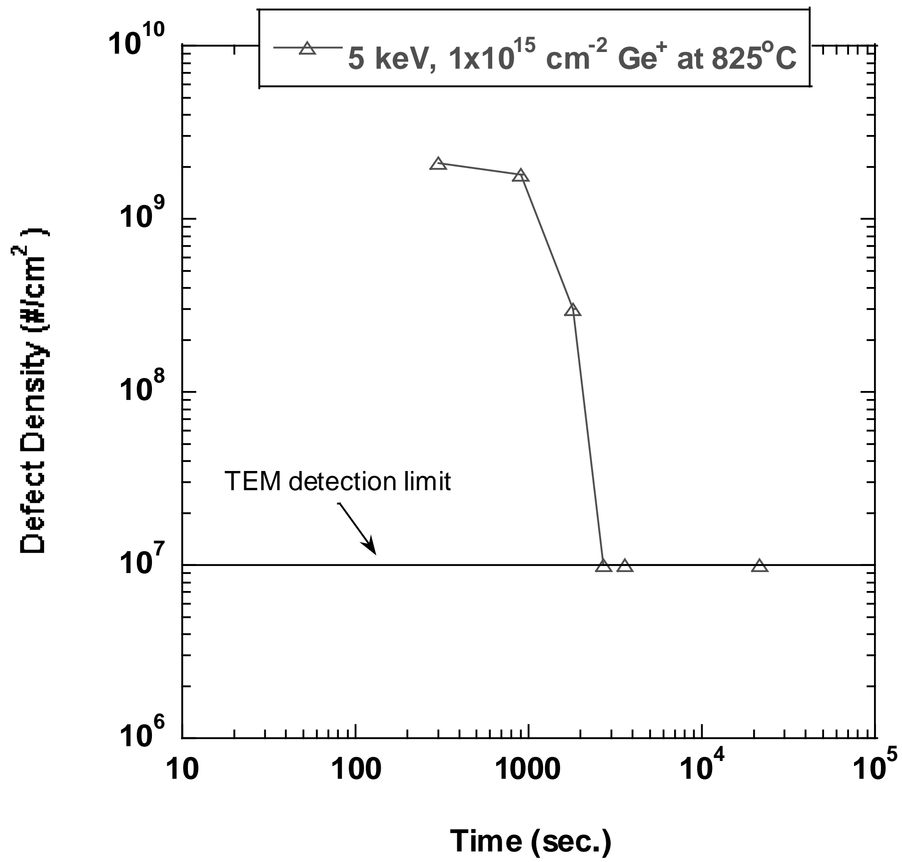

Figure 3.8 Defect evolution from 5 keV, $1x10^{15}$ cm^{-2} Ge^+ implant at 825 °C.

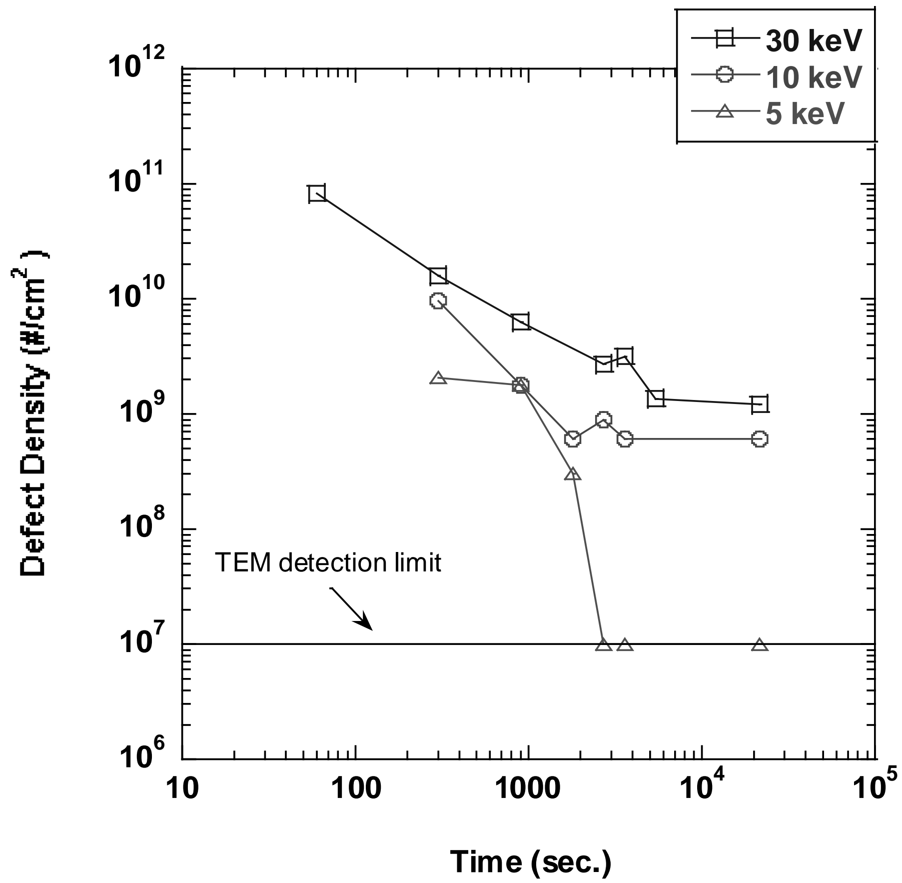

Figure 3.9 Combined defect density evolution for the 5, 10 and 30 keV $1x10^{15}$ cm^{-2} Ge^{+} samples annealed at 825 °C.

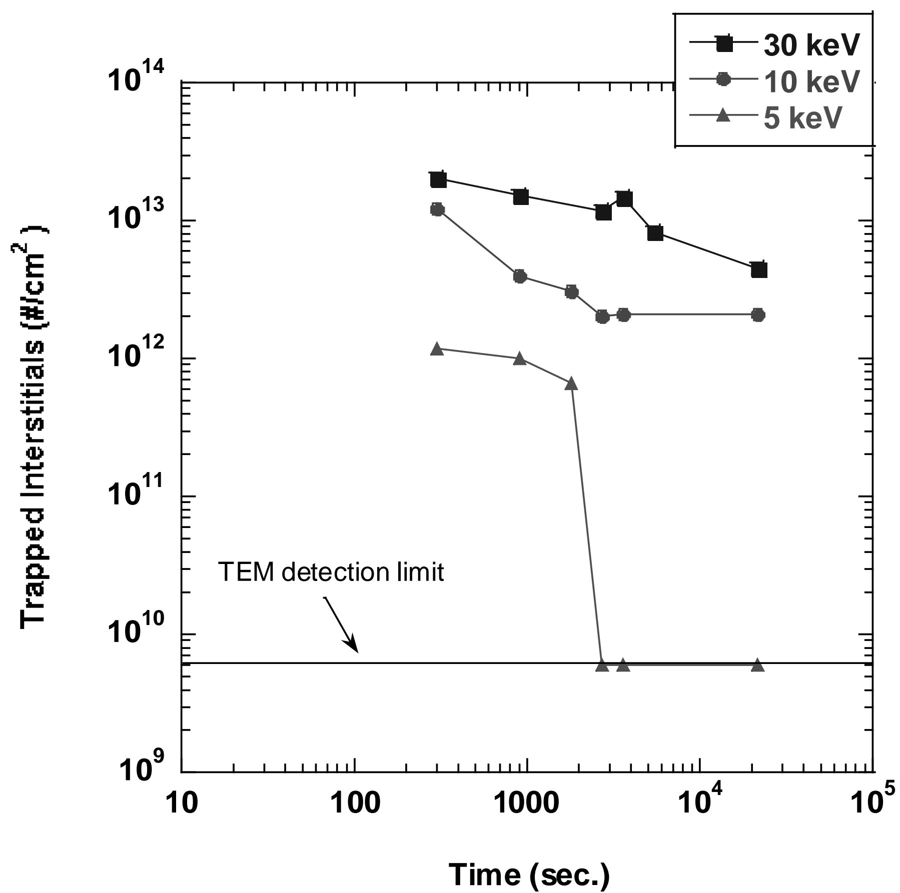

Figure 3.10 Trapped interstitials for defects from 5, 10 and 30 keV 1x10^{15} cm^{-2} Ge^+ implant annealed at 825 °C.

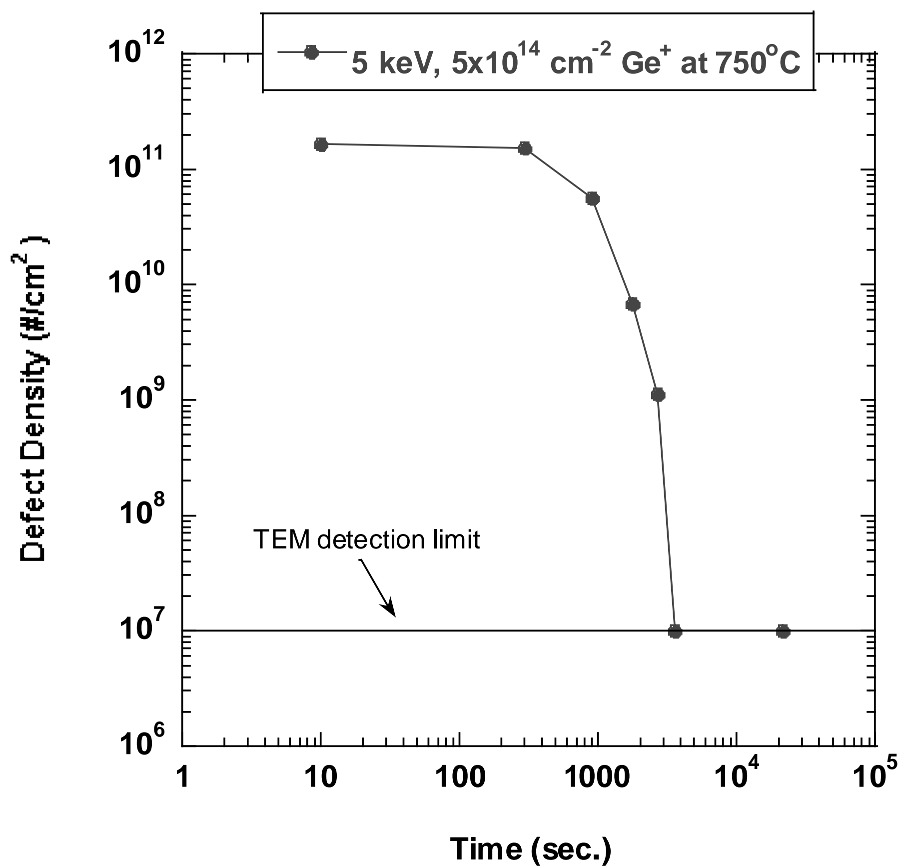

Figure 3.11 Defect evolution from a 5 keV, $5x10^{14}$ cm^{-2} Ge^+ implant on silicon.

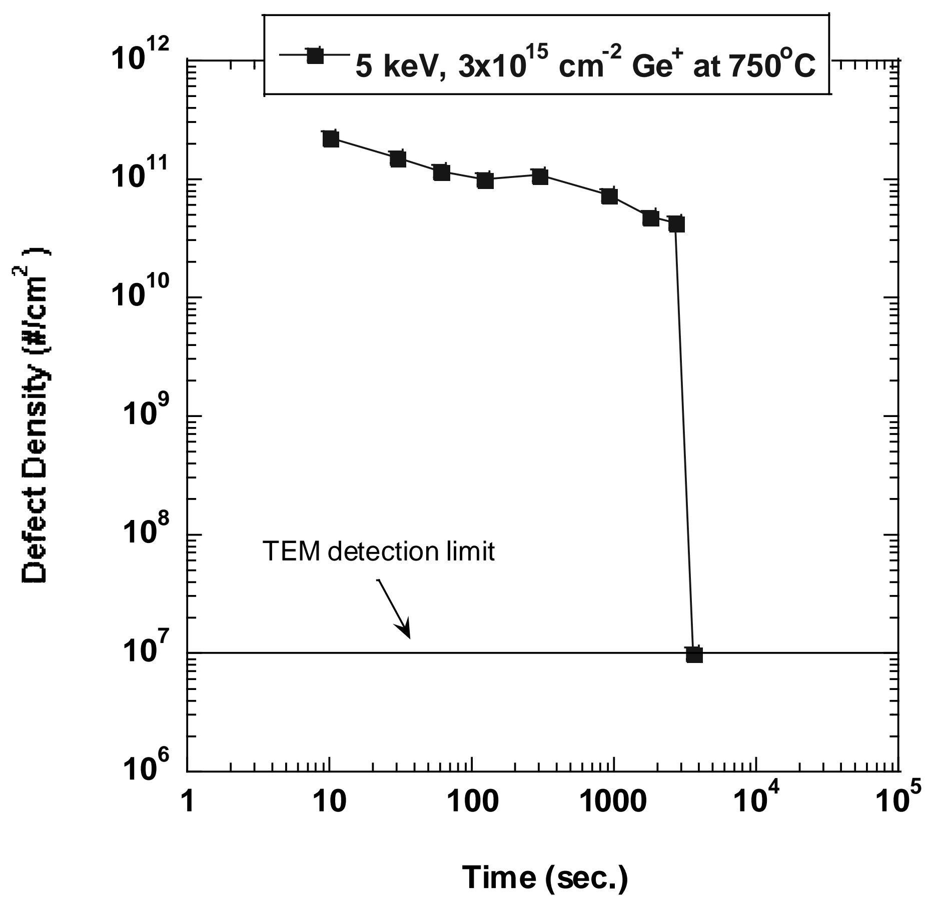

Figure 3.12 Defect evolution from a 5 keV, 3×10^{15} cm^{-2} Ge^{+} implant on silicon.

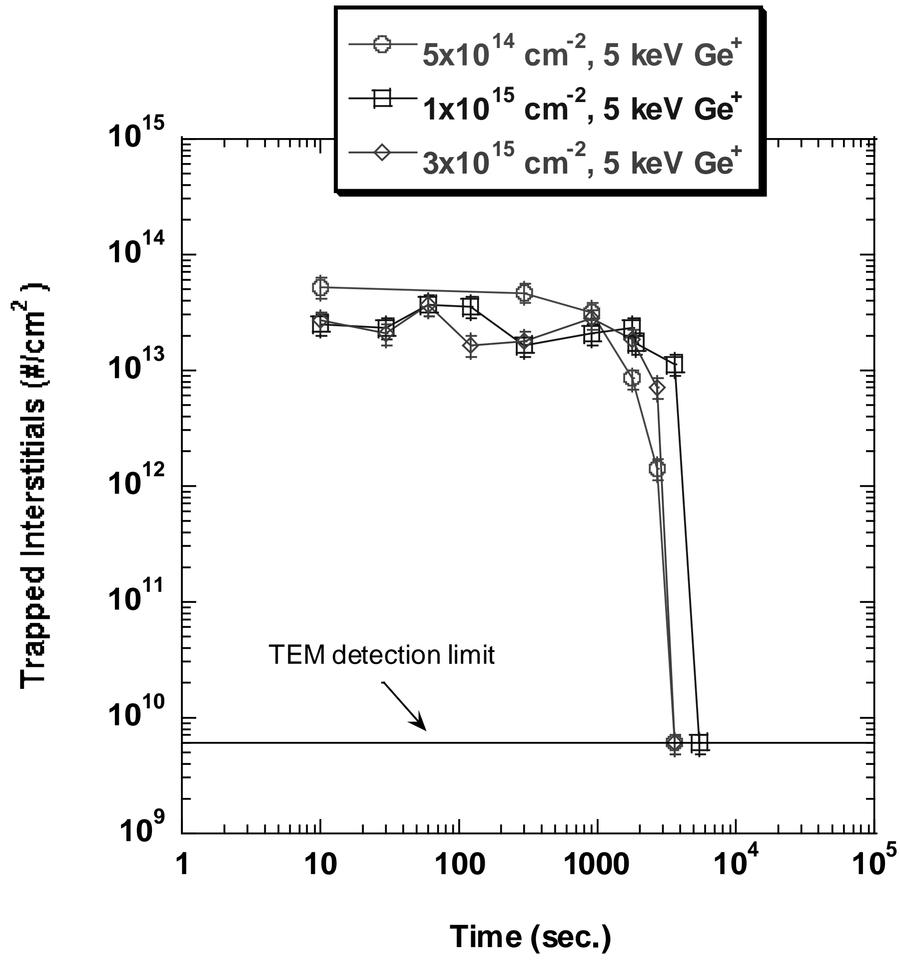

Figure 3.13 Trapped interstitials for defects from 5 keV, $5x10^{14}$, $1x10^{15}$ and $3x10^{15}$ cm^{-2} Ge^{+} implants annealed at 750 °C.

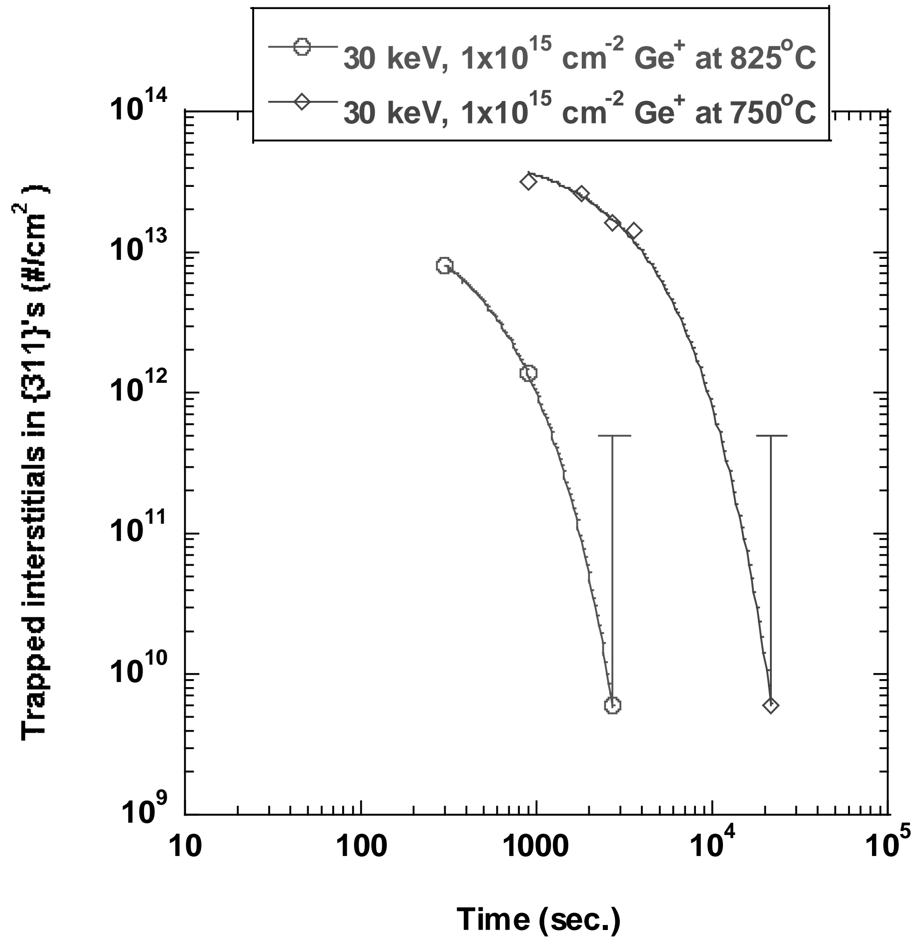

Figure 3.14 Trapped interstitials in {311} type defects for 30 keV, $1x10^{15}$ cm^{-2} Ge^+ implants at 750 °C and 825 °C.

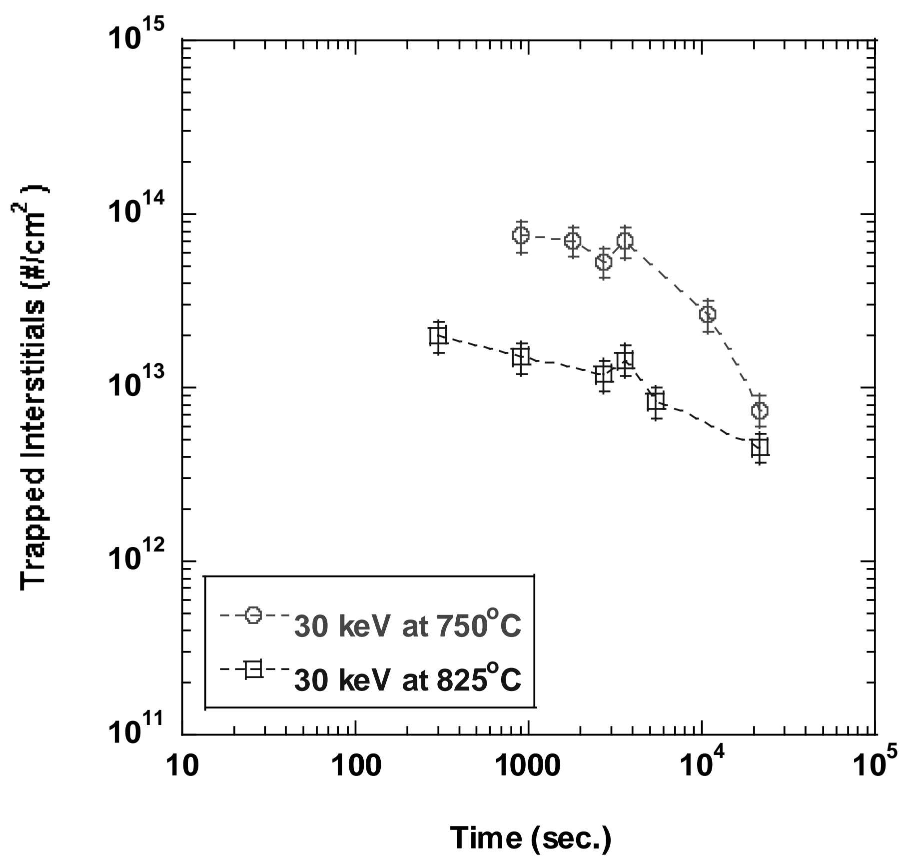

Figure 3.15 Trapped interstitials resulting from 30 keV, $1x10^{15}$ cm^{-2} Ge^{+} implants at 750 and 825 °C.

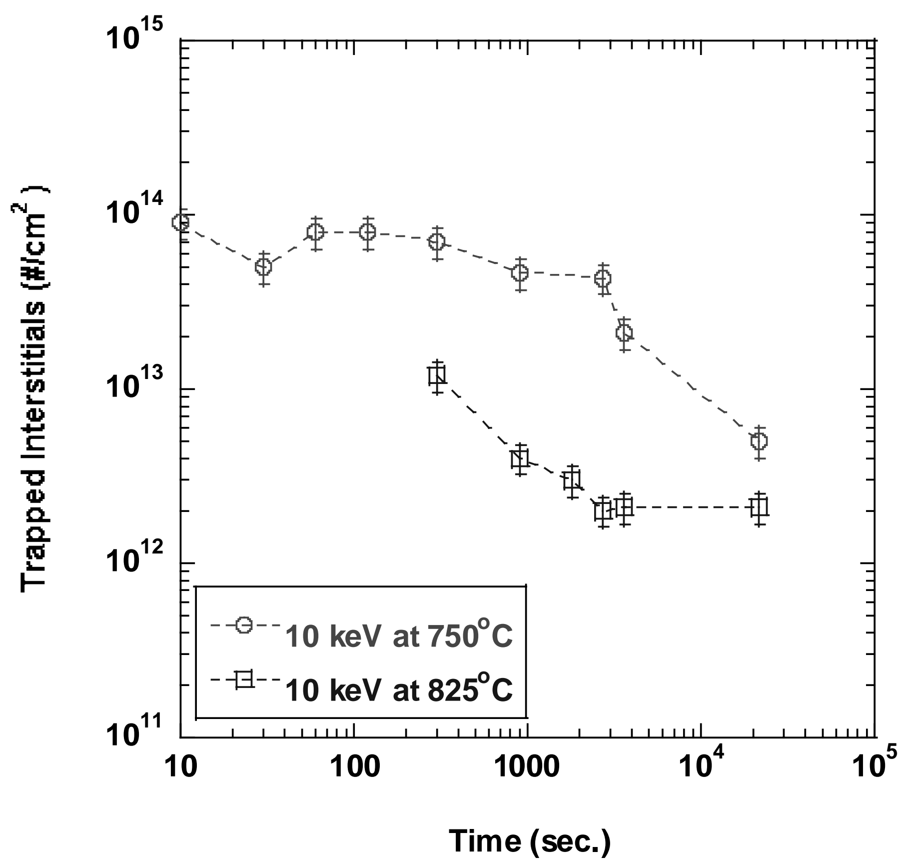

Figure 3.16 Trapped interstitials resulting from 10 keV, $1x10^{15}$ cm^{-2} Ge^{+} implants at 750 and 825 °C.

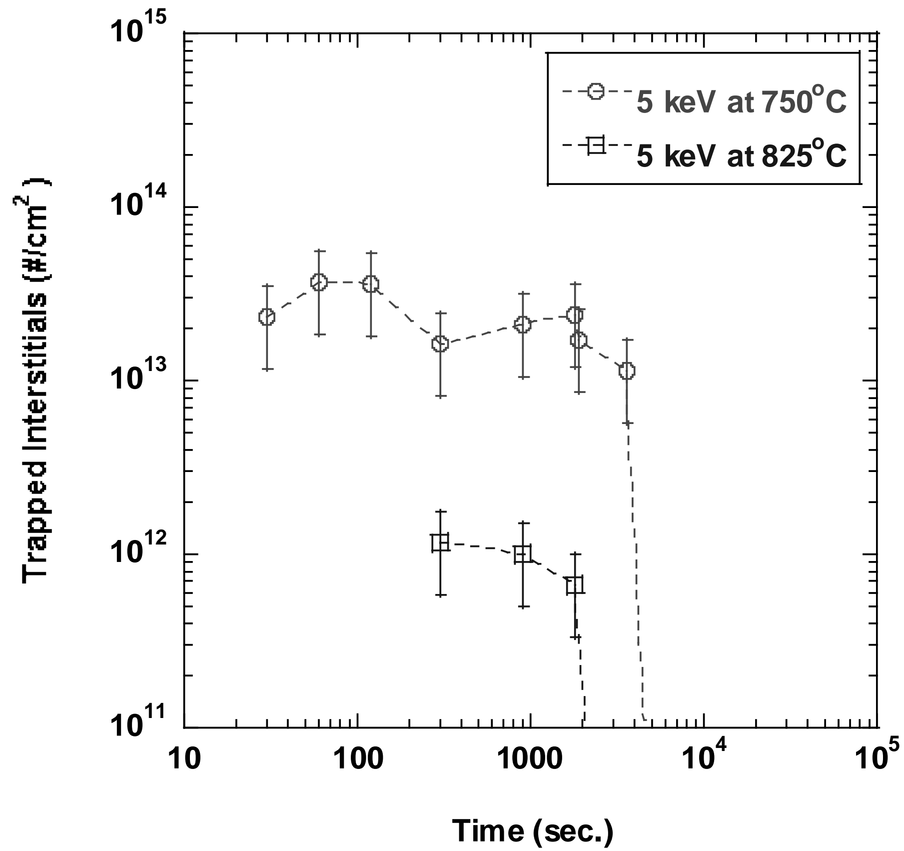

Figure 3.17 Trapped interstitials resulting from 5 keV, $1x10^{15}$ cm^{-2} Ge^{+} implants at 750 and 825 °C.

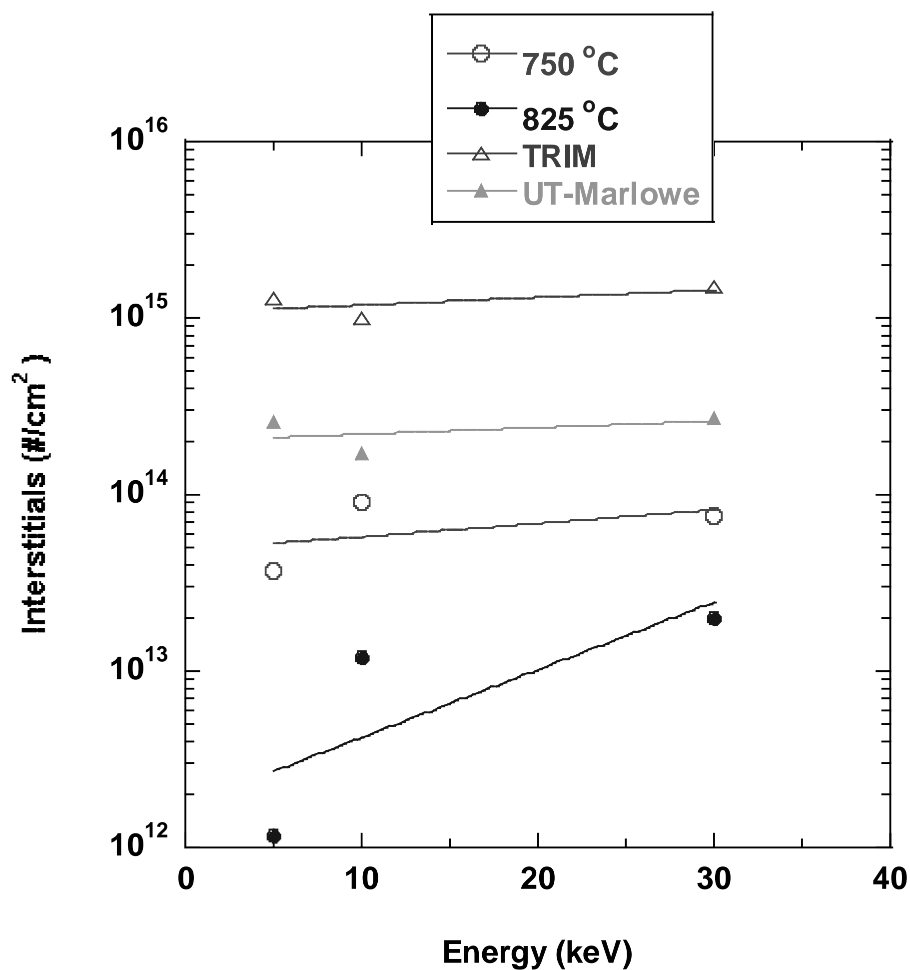

Figure 3.18 Empirical and simulated values for the excess interstitials following implantation with Ge^{+} at 5, 10 and 30 keV given by experimental results and the SRIM2000 and UT-Marlowe simulations.

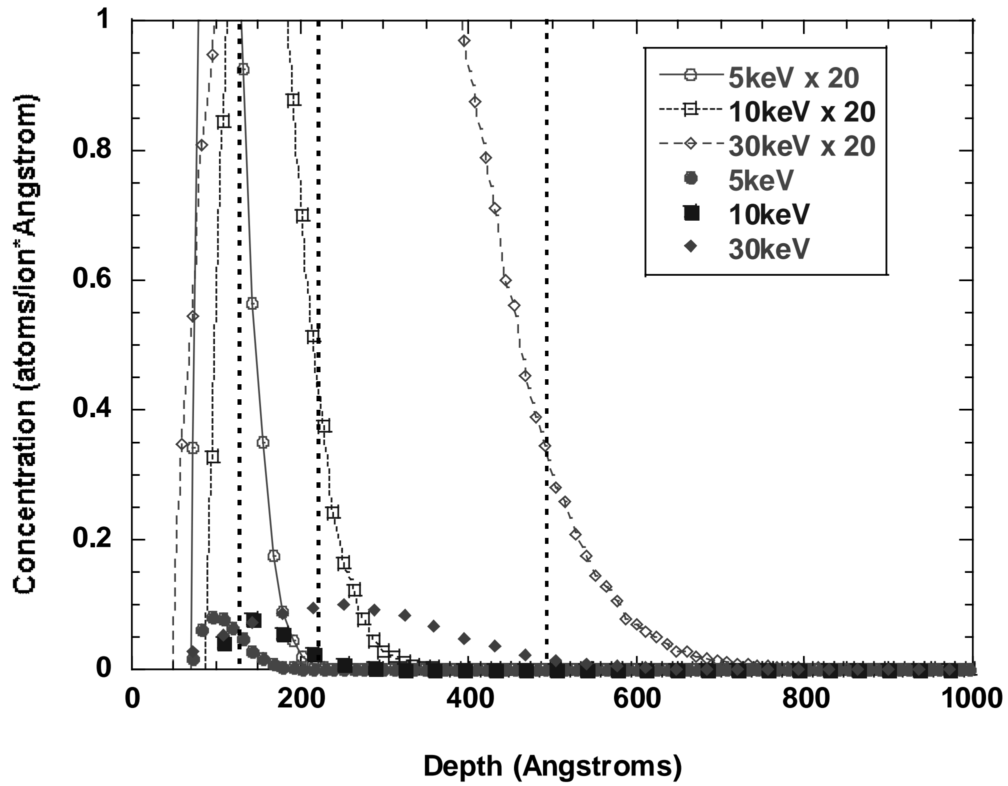

Figure 3.19 Implant profile curves given by TRIM simulation for the 5, 10 and 30 keV energies. The dashed lines depict the depth of the amorphous/crystalline layers.

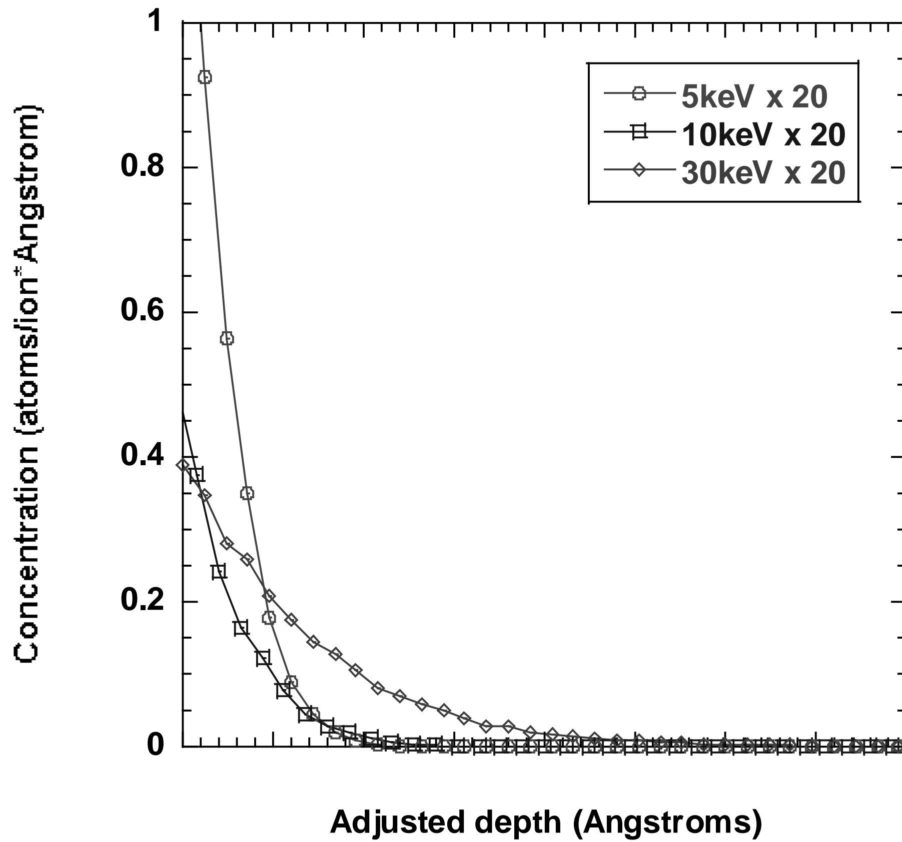

Figure 3.20 Comparison of implant profile for each energy x20. The horizontal ordinate has been adjusted for each profile so that the zero point on the axis signifies the amorphous/crystalline depth 120, 220 and 480 Å, respectively for increasing energy.

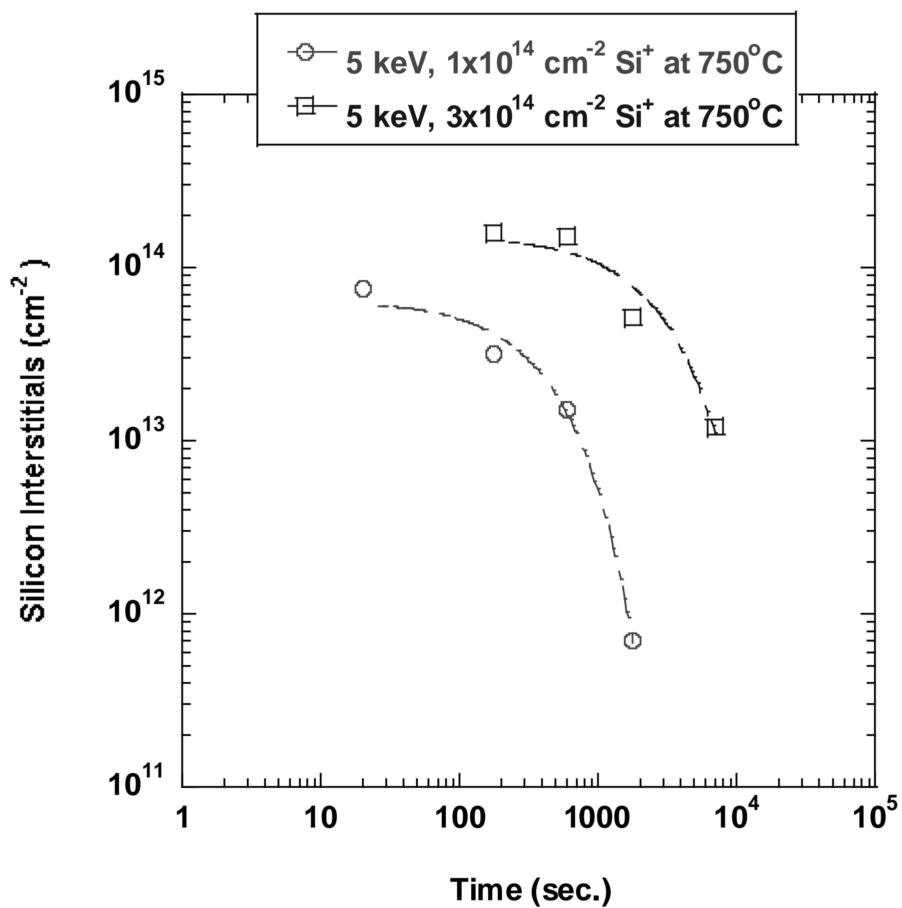

Figure 3.21 Dose dependence for low energy, 5 keV Si^+ implants annealed at 750 °C, as reported by Agarwal et al. [20].

CHAPTER 4
CONCLUSIONS AND FUTURE WORK

4.1 Conclusions

Future device dimension down scaling will depend, among other factors, on whether certain challenges in the formation of ultra shallow junctions will be overcome; hence this topic occupies a critical position in most technology roadmaps. The required low resistivity, highly doped structures will mandate improvements in the understanding of the microstructural behavior after ion implantation and subsequent annealing treatments.

This work has studied the effects of implant energy, dose and temperature on the evolution of defects resulting from amorphizing germanium implants in silicon. No dopants were used in the experiments so that only the damage caused by the implantation process was studied. Hence, the variation of the parameters mentioned above provided an adequate source of comparison when characterizing the damage induced. Particularly interesting was the behavior of defects at the technologically important, low energy regime (< 5 keV), the one required for the formation of ultra shallow junctions.

The first experiment compared the defect evolution of three energies (i.e., 5, 10 and 30 keV), at a fixed dose of 1×10^{15} cm^{-2}, upon annealing at 750 °C in N_2. At this temperature the following defect behavior was observed. For the 30keV, the expected initial growth and coexistence of {311}'s and dislocation loops eventually gave way to

the dissolution of {311}'s with time and the presence of large, stable dislocation loops. For the 10 keV, only dislocation loops were observable from the PTEM micrograph images, and these seemed to undergo a coarsening process with time which decreased defect density but increased defect size. For the 5 keV, again only dislocation loops were observed from the PTEM micrograph images, but these were small in size and completely dissolved within a narrow time window, a behavior not observed in other studies and indicative of their instability.

Increasing the annealing temperature to 825 °C and repeating the same experiment yielded very similar trends. The defect density of the 30 and 10 keV energy samples seemed to leveled off at $5x10^{12}$ and $2x10^{12}$ defects/cm^{-2}, respectively. However at the 5 keV implant energy, the defect density plummeted beyond the sensitivity of the TEM within a narrow time window. These results apparently point to a threshold of defect stability dependent on implant energy. Above 10 keV, defects remain in the microstructure and achieve some degree of stability, evidenced by their presence even after long anneals. At 5 keV though, defect stability sharply decreases as evidenced by the rapid dissolution of the small dislocation loops present in the microstructure.

Lastly, a dose comparison experiment was carried out at 750 °C for this low implant energy to determine dose dependence on defect evolution. For the three doses chosen, $5x10^{14}$, $1x10^{15}$ and $3x10^{15}$ cm^{-2}, no significant difference was observed in the defect behavior over time. All three doses showed similarly sharp drops in defect density and number of trapped interstitials, to the TEM detection limit, within a narrow time frame.

These results, together with the temperature experiments indicate the following conclusions. For germanium-implanted silicon, temperature does not have a significant qualitative difference on defect evolution trends. Similarly, dose does not have a significant qualitative or quantitative difference on defect evolution. In contrast, defect behavior over time shows a heavy dependence on implant energy. Finally, the fact that {311}'s do not form at the lowest energy, only small, unstable dislocation loops, point to an alternate path of interstitial evolution where {311} formation from the initial clusters does not take place. Figure 4.1 illustrates this conclusion for low energy germanium implants in silicon. The highlighted path reflects the results of this study.

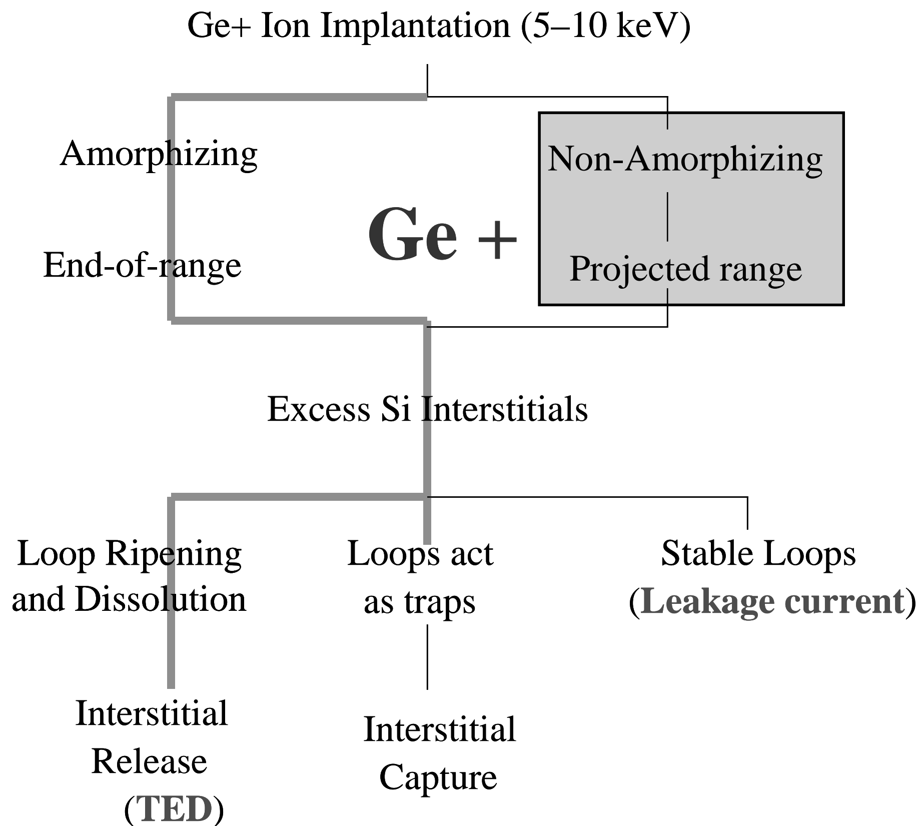

Figure 4.1 Alternate path of interstitial evolution from low energy germanium implants.

4.2 Future Work

Further work in defect and interstitial behavior from low energy germanium implants would enhance the understanding of the driving forces behind such behavior. Specifically, the role of the surface becomes an important parameter in the low energy regime, since the implant damage is so shallow and interstitial recombination at the surface could take place.

To determine this, a simple CMP (chemical-mechanical planarization) experiment should be carried out. By polishing the surface of a 10 keV energy sample roughly 100 Å, the depth of the amorphous layer would be equivalent to that of the 5 keV sample. Upon annealing of this polished specimen, if the defect evolution follows the leveling off trend of the non-polished 10 keV samples, then surface proximity does not play a role in interstitial evolution. However, if the defect evolution follows the sharp drop in density seen in the non-polished 5 keV samples, then the role of the surface would be a contributing variable to this evolution.

Expanding this study to more temperatures and times will yield a comprehensive experimental basis for future model development work. Specifically, very short anneal times using a rapid thermal annealing (RTA) furnace are necessary with increasing temperature. These anneals would have been useful for the 825 °C experiment and would have yielded a more accurate picture of defect evolution.

APPENDIX
PTEM IMAGES FOR THE ENERGY AND DOSE DEPENDENCE STUDIES

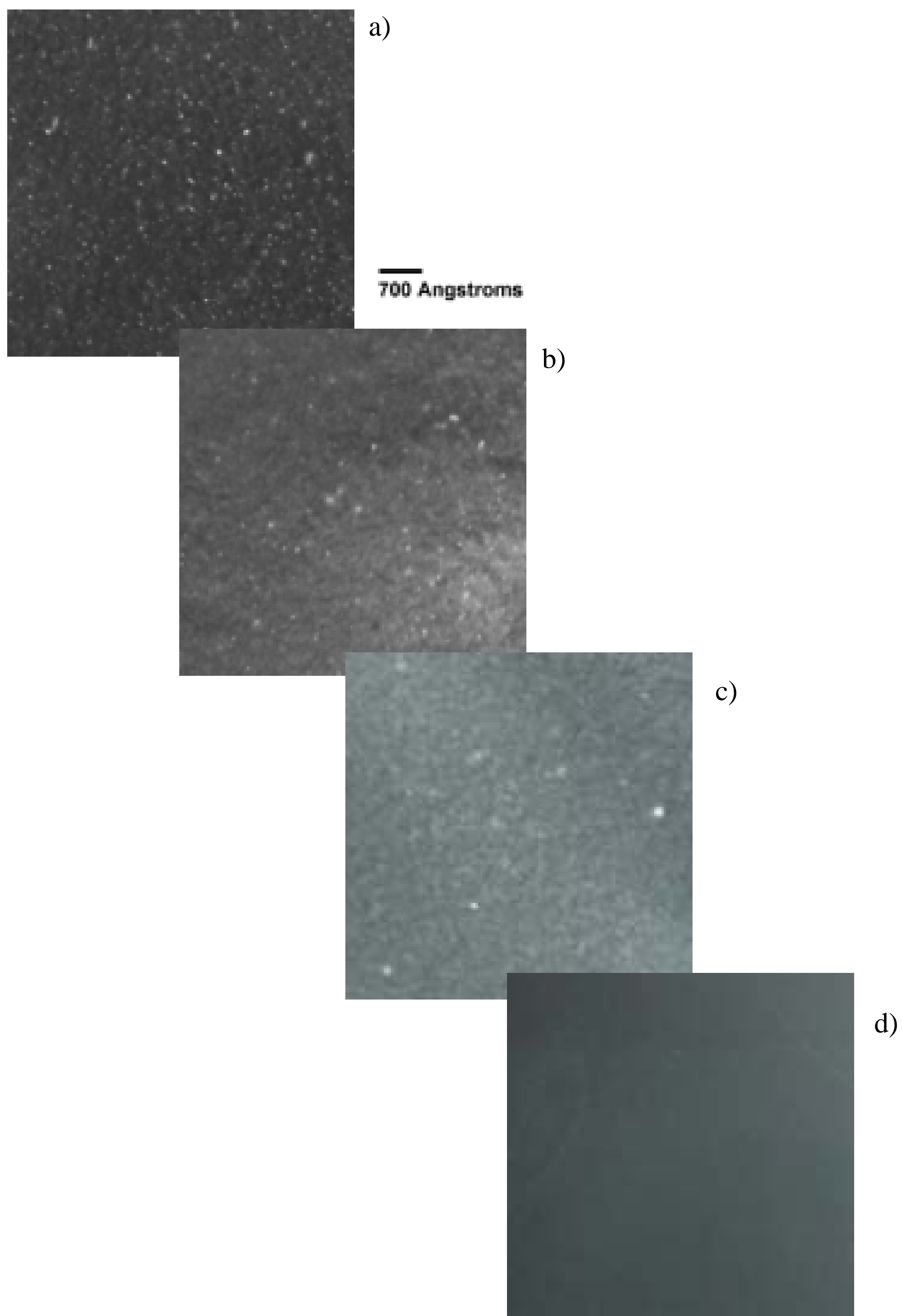

Figure A.1 PTEM micrographs of the 5 keV, $1x10^{15}$ cm^{-2} Ge^{+} annealed at 750 °C for a) 5 min. b) 15 min. c) 60 min. and d) 360 min.

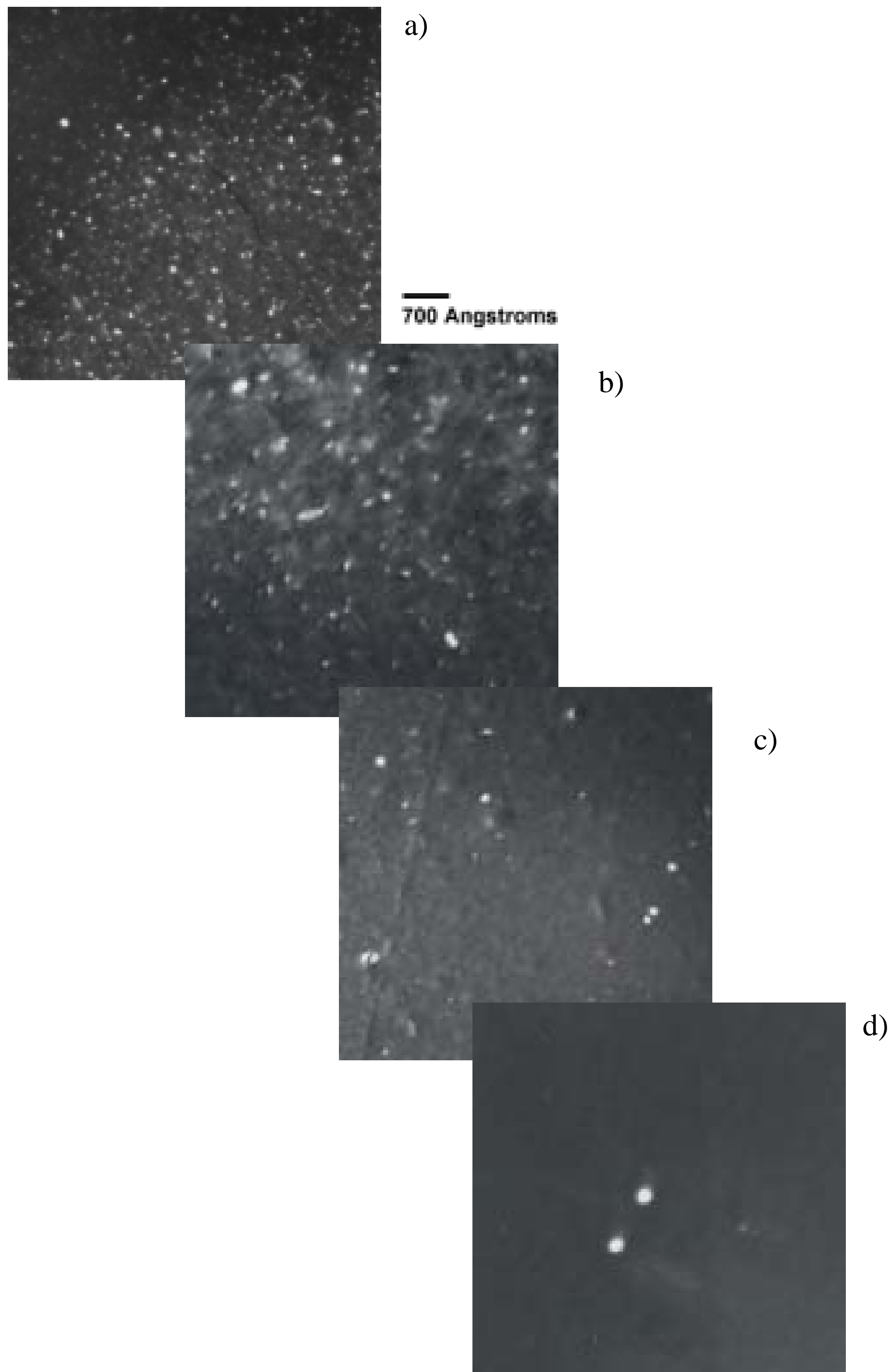

Figure A.2 PTEM micrographs of 10 keV, $1x10^{15}$ cm^{-2} Ge^{+} annealed at 750 °C for a) 2 min. b) 15 min. c) 60 min and d) 360 min.

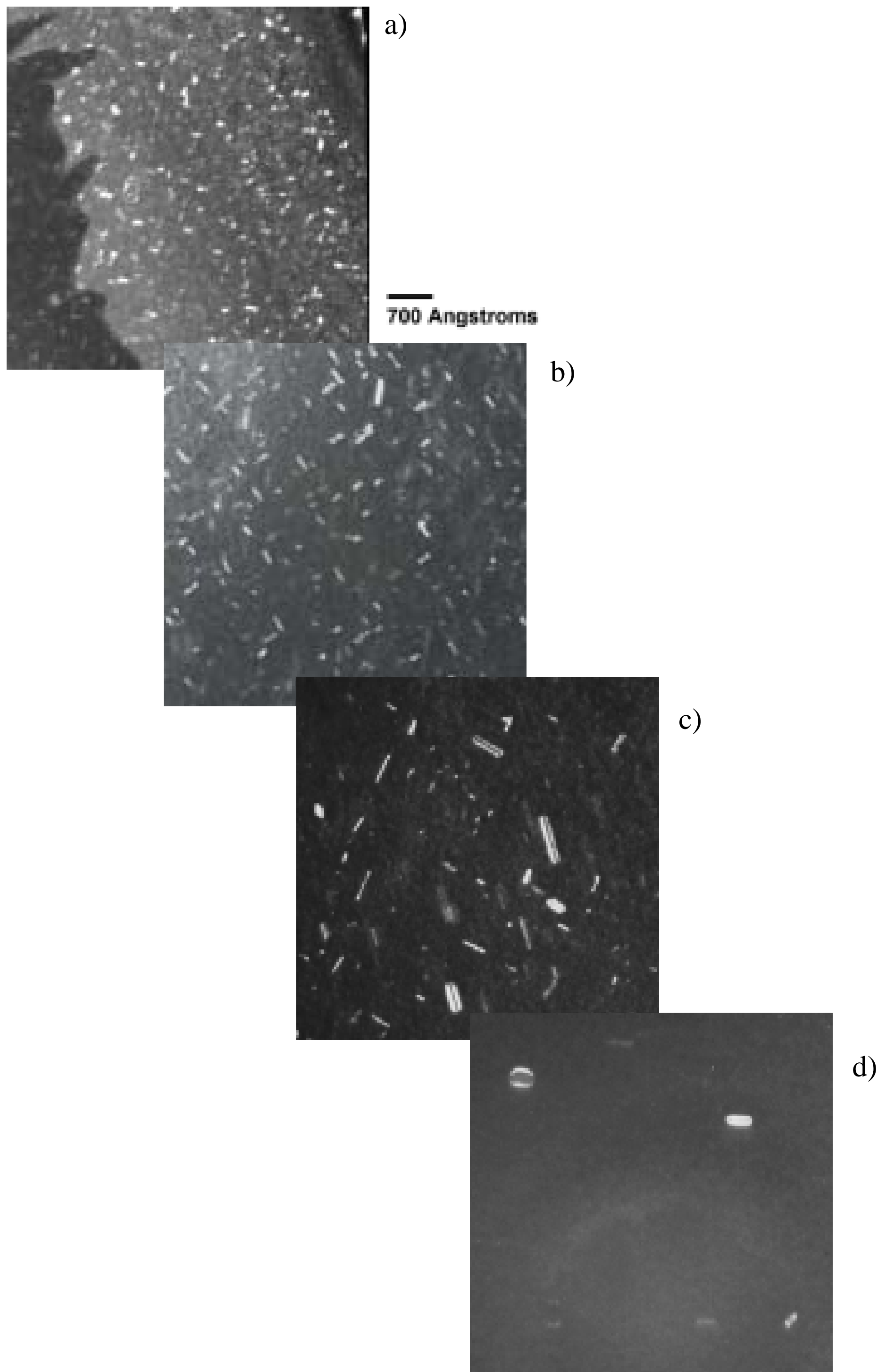

Figure A.3 PTEM micrographs of 30 keV, $1x10^{15}$ cm^{-2} Ge^{+} annealed at 750 °C for a) 2 min. b) 15 min. c) 60 min and d) 360 min.

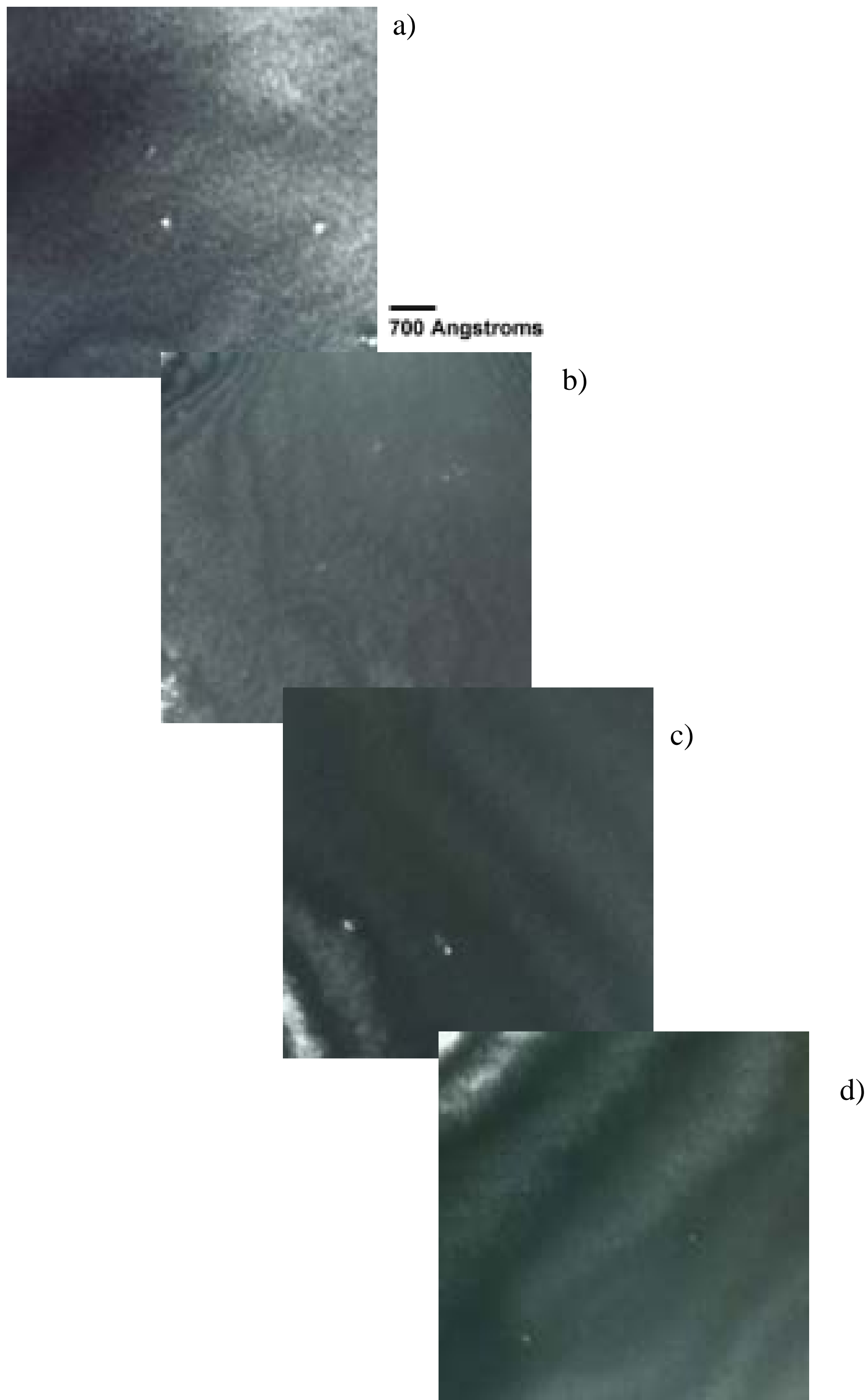

Figure A.4 PTEM micrographs of 5 keV, $1x10^{15}$ cm^{-2} Ge^{+} annealed at 825 °C for a) 5 min. b) 15 min. c) 30 min and d) 45 min.

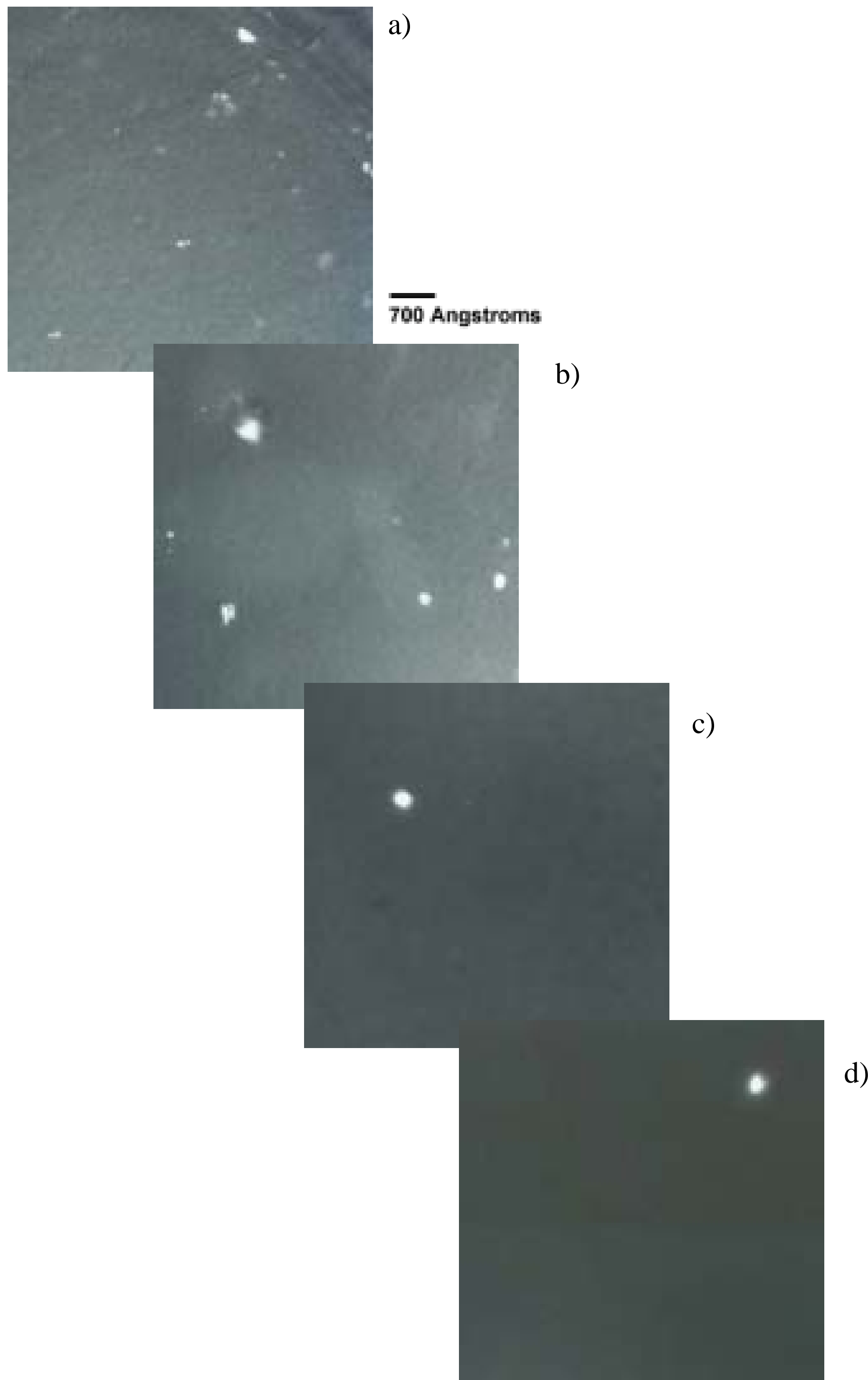

Figure A.5 PTEM micrographs of 10 keV, $1x10^{15}$ cm^{-2} Ge^{+} annealed at 825 °C for a) 5 min. b) 15 min. c) 30 min and d) 60 min.

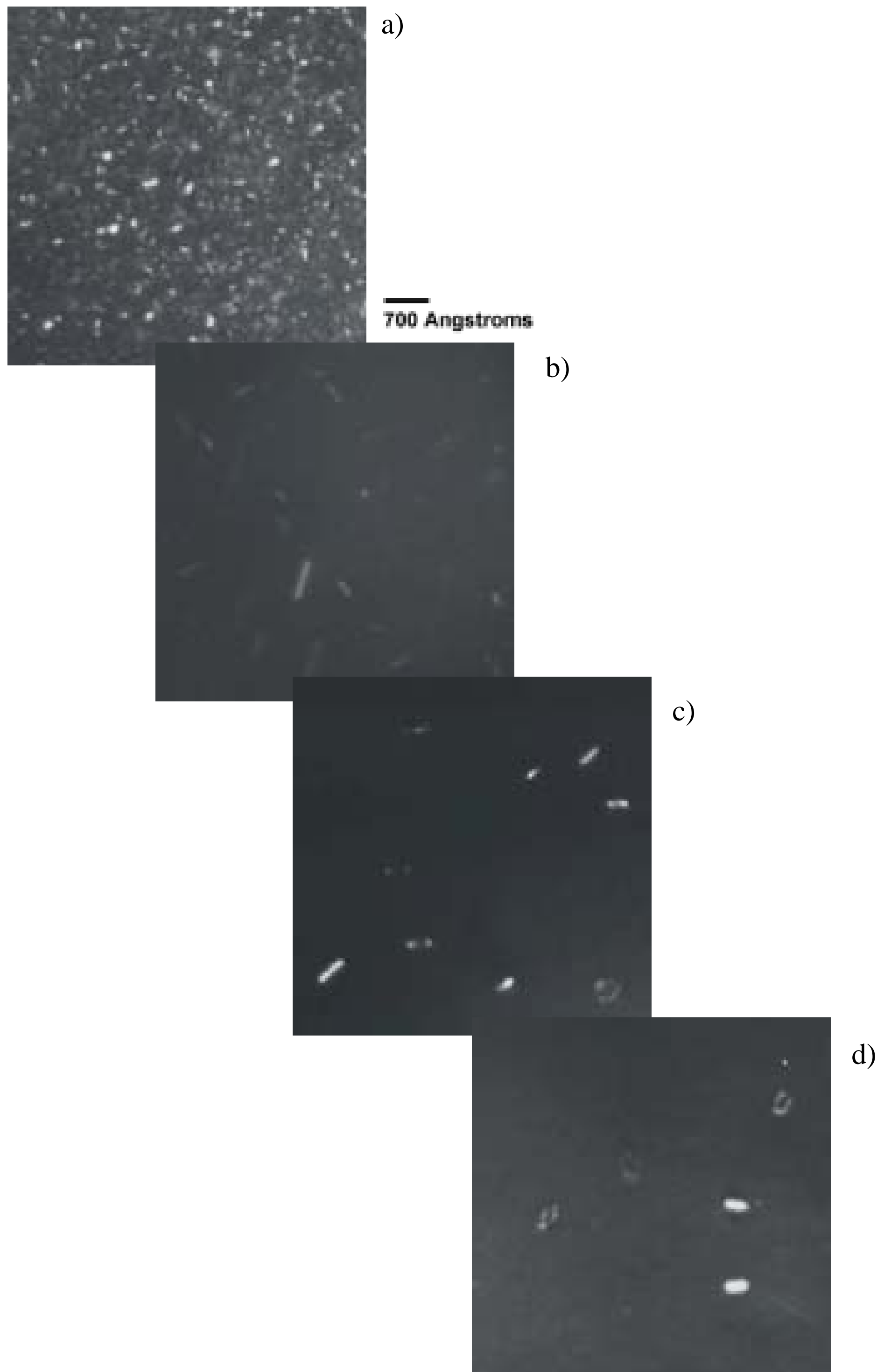

Figure A.6 PTEM micrographs of 30 keV, $1x10^{15}$ cm^{-2} Ge^{+} annealed at 825 °C for a) 1 min. b) 5 min. c) 15 min and d) 60 min.

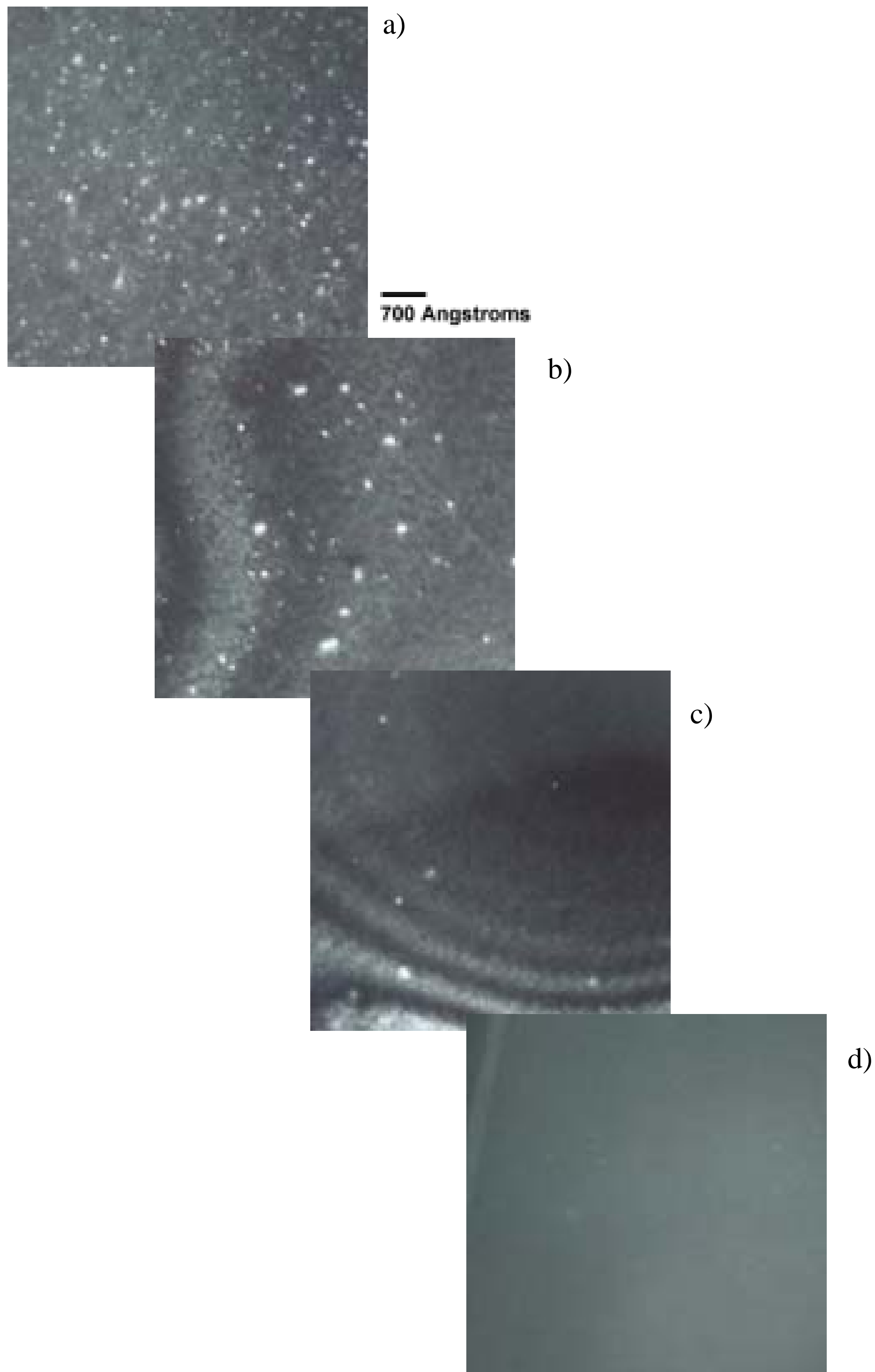

Figure A.7 PTEM micrographs of 5 keV, $5x10^{14}$ cm^{-2} Ge^{+} annealed at 750 °C for a) 5 min. b) 15 min. c) 30 min and d) 360 min.

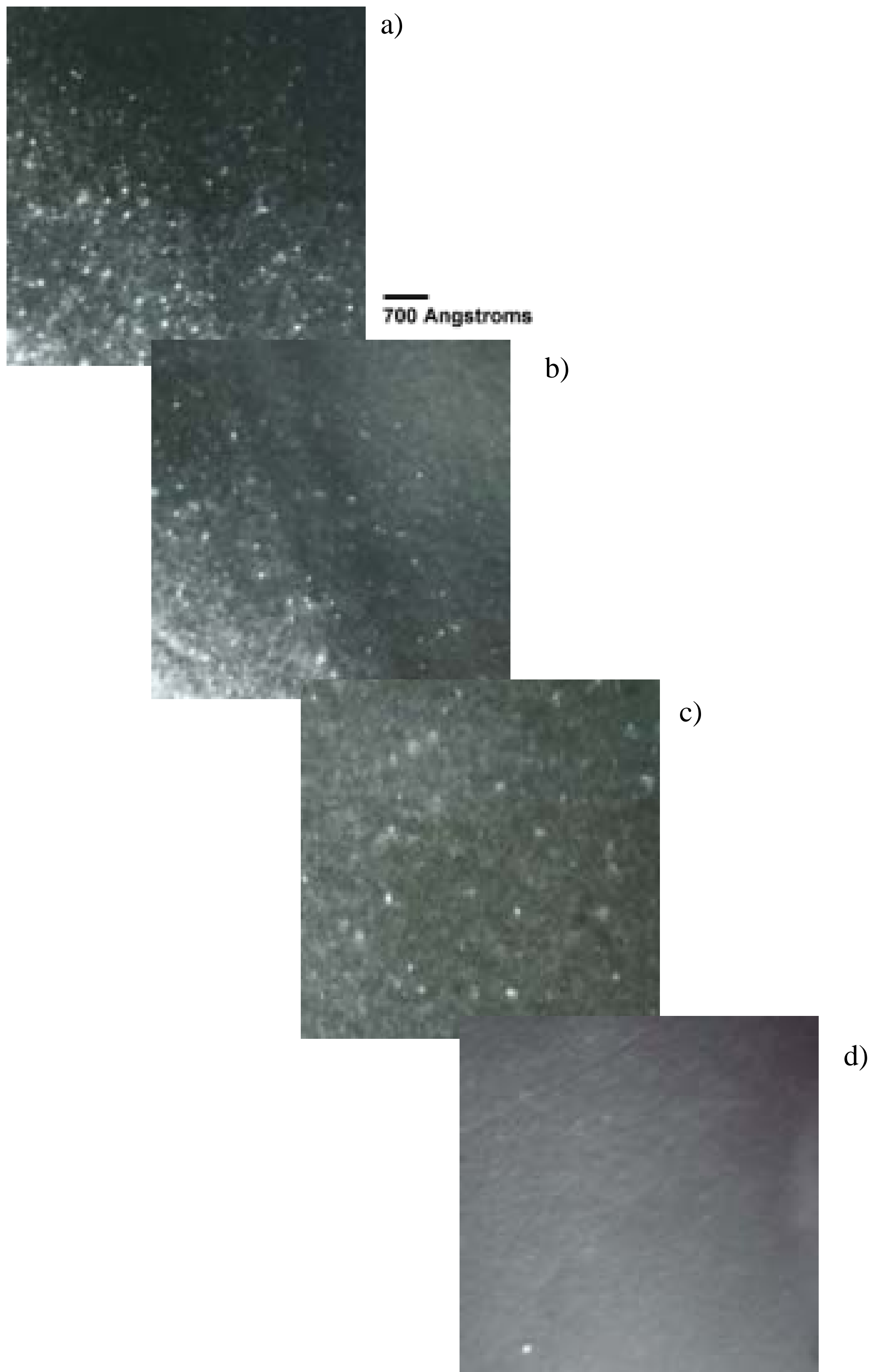

Figure A.8 PTEM micrographs of the 5 keV, $3x10^{15}$ cm^{-2} Ge^{+} annealed at 750 °C for a) 5 min. b) 15 min. c) 30 min. and d) 60 min.

LIST OF REFERENCES

1. Neil H. E. Weste and Kamran Eshraghian, *Principles of CMOS VLSI Design*. second ed. 1993: New York, Addison-Wesley Publishing Co.

2. SIA, *International Technology Roadmap for Semiconductors*, 1999, Semiconductor Industry Assoc.: San Jose, CA.

3. Yuan Taur, *The Incredible Shrinking Transistor*, in *IEEE Spectrum*. July 1999. p. 25-29.

4. Badih El-Kareh, *Fundamentals of Semiconductor Processing Technologies*. 1995: Boston, Kluwer Academic Publishers.

5. M. A. Foad, A. J. Murrell, E. J. H. Collart, G. de Cock, D. Jennings and M. I. Current, Mat. Res. Soc. Symp. Proc., 1999. **568**: p. 55-63.

6. G. A. Kachurin, V. A. Mayer, S. I. Romanov, M. Voelskow, R. Klabes and E. Wieser, Phys. Stat. Sol. (a), 1984. **82**: p. 475-480.

7. Kevin S. Jones and Jozsef Gyulai, in *Ion Implantation Science and Technology*, J.F. Ziegler, Editor. 1996: New York, Ion Implantation Technology Co. p. 239-261.

8. SIA, *International Technology Roadmap for Semiconductors*, 1997, Semiconductor Industry Assoc.: San Jose, CA.

9. D. K. Brice, Radiation Effects, 1970. **6**: p. 77-87.

10. E. Glaser, G. Gotz, N. Sobolev and W. Wesch, Phys. Stat. Sol., 1982. **69**: p. 603-614.

11. Siegfried Mader, in *Ion Implantation Science and Technology*. 1988: Boston, Academic Press. p. 109-138.

12. Jack Washburn, in *Defects in Semiconductors*, Narayan and Tan, eds. 1981: Boston, North-Holland Inc. p. 209-223.

13. Kevin S. Jones, S. Prussin and E. R. Weber, Appl. Phys. A, 1988. **45**: p. 1-34.

14. T. Y. Tan, *Atomic Modeling of Homogeneous Nucleation of Dislocations from Condensation of Point Defects in Silicon*, in *Philosophical Magazine*. 1981. p. 101-125.

15. J. L. Benton, S. Libertino, P. Kringhoj, D. J. Eaglesham, J. M. Poate and S. Coffa, J. Appl. Phys., 1997. **82**(1): p. 120-125.

16. R. Drosd and J. Washburn, J. Appl. Phys., 1982. **53**(1): p. 397-403.

17. S. Prussin and Kevin S. Jones, J. Electrochem. Soc., 1990. **137**(6): p. 1912-1914.

18. Lance S. Robertson, Aaron Lilak, Mark E. Law, Kevin S. Jones, Per S. Kringhoj, Leonard M. Rubin, John Jackson, David S. Simons and Peter Chi, Appl. Phys. Lett., 1997. **71**(21): p. 3105-3107.

19. K. S. Jones, K. Moller, J. Chen, M. Puga-Lambers, B. Freer, J. Berstein and L. Rubin, J. Appl. Phys., 1997. **81**(9): p. 6051-6055.

20. Aditya Agarwal, Tony E. Haynes, David J. Eaglesham, Hans-J. Gossmann, Dale C. Jacobson, John M. Poate and Yu E. Erokhin, Appl. Phys. Lett., 1997. **70**(23): p. 3332-3334.

21. D. J. Eaglesham, P. A. Stolk, H.-J. Gossmann, T. E. Haynes and J. M. Poate, Nucl. Instr. and Meth. in Phys. Res. B, 1995. **106**: p. 191-197.

22. Jinghong Li and Kevin S. Jones, Appl. Phys. Lett., 1998. **73**(25): p. 3748-3750.

23. Alain Claverie, Benjamin Colombeau, Gerard Ben Assayag, Caroline Bonafos, Filadelfo Cristiano, Mourad Omri and Bernadette de Mauduit, Mat. Sci. in Semic. Proc. 2000. **3**: p. 269.

24. J. R. Liefting, J. S. Custer and F. W. Saris, Mat. Sci. and Eng., 1994. **B25**: p. 60.

25. C. Bonafos, D. Mathiot and A. Claverie, J. Appl. Phys., 1998. **83**(6): p. 3008-3017.

26. D. J. Eaglesham, P. A. Stolk, H.-J. Gossmann and J. M. Poate, Appl. Phys. Lett., 1994. **65**(18): p. 2305-2307.

27. K. S. Jones, J. Liu, L. Zhang, V. Krishnamoorthy and R. T. DeHoff, Nucl. Instr. and Meth. in Phys. Res. B, 1995. **106**: p. 227-232.

28. N. E. B. Cowern, G. Mannino, F. Roozeboom, P. A. Stolk, H. G. A. Huizing, J. G. M. van Berkum, N. N. Toan and P. H. Woerlee. In *195th ECS Meeting*. 1999. Seattle, WA.

29. D. J. Eaglesham, A. Agarwal, T. E. Haynes, H.-J. Gossmann, D. C. Jacobson and J. M. Poate, Nuclear Instruments and Methods in Physics Research B, 1996. **120**: p. 1-4.

30. M. E. Law and S. M. Cea, Computational Materials Science, 1998. **12**: p. 289-308.

31. E. Schroer, V. Privitera, F. Priolo, E. Napolitani and A. Camera, Appl. Phys. Lett., 2000. **76**(21): p. 3058-3060.

32. A. E. Michel, Nucl. Instr. and Meth. in Phys. Res. B, 1989. **37/38**: p. 379-383.

33. P. A. Packan and J. D. Plumer, Appl. Phys. Lett., 1990. **56**: p. 1787-1789.

34. Aditya Agarwal. in *13th International Conference on Ion Implantation Technology*. 2000. Alpbech, Austria: In press.

35. E. Myers, G. A. Rozgonyi, D. K. Sadana, W. Maszara, J. J. Wortman and J. Narayan, Mat. Res. Soc. Symp. Proc., 1985. **(Preprint)**.

36. Mehmet C. Ozturk, Jimmie J. Wortman, Carlton M. Osburn, Atul Ajmera, George A. Rozgonyi, Eric Frey, Wei-Kan Chu and Clinton Lee, IEEE Transactions on Electron Devices, 1988. **35**(5): p. 659-667.

37. A. C. Ajmera and G. A. Rozgonyi, Appl. Phys. Lett., 1986. **49**(19): p. 1269-1271.

38. K. L. Lee, T. Zabel, P. M. Kozlowski, R. Viswanathan and K. Chen, Mat. Res. Soc. Symp. Proc., 1999. **568**: p. 37-42.

39. Christian Camarce, *Effects of Surface Proximity on {311} Defect Kinetics and Transient Enhanced Diffusion*, in *Department of Materials Science and Engineering*. Master's Thesis, May 2000, University of Florida: Gainesville. p. 109.

40. B. Obradovic, G. Wang, Y. Chen, D. Li, C. Snell and A. F. Tasch, *UT-Marlowe 5.0*, 1999: University of Texas, Austin; Los Alamos National Laboratory.

41. Jinning Liu, Kevin S. Jones, Daniel F. Downey and Sandeep Mehta, Mat. Res. Soc. Symp. Proc., 1999. **568**: p. 9-14.

42. E. Ganin and A. Marwick, Mat. Res. Soc. Symp. Proc., 1989. **147**: p. 13-18.

BIOGRAPHICAL SKETCH

Born in Bogota, Colombia, in 1977, the author moved two years later, with his family, to Madrid, Spain, where he spent six years. In May 1985, the author's family moved to the United States and took residence in South Florida. There, he graduated as salutatorian of his high school class a decade later. That year he enrolled at the University of Florida where he earned a B.S. degree in materials science and engineering in May 2000 as part of a joint B.S./M.S. degree program. He continued his education with the Department, which led to an M.S. degree in May 2001.

The author has had the blessing of traveling to many countries including Colombia, Spain, Peru, Italy, France, Australia, and Israel. His hobbies include playing the piano, sports and spending time with family. In August 2001, the author will begin a job as a rotation engineer for Intel Corp. in Chandler, AZ, where he interned for two semesters in 1998.